Highlights

Numerical and Experimental Hydrodynamic Assessment of a Dihedral Bulbous Bow Retrofit for a Semi-Planing Fishing Vessel

H. R. Díaz-Ojeda, Yifu Zhang, Tahsin Tezdogan, Francisco Pérez Arribas

- Dihedral bulbous bow achieves 28–32% resistance reduction at semi-planing speeds ($Fr > 0.38$)
- Combined pressure reduction and trim modification mechanisms validated through EFD-CFD approach
- Critical speed thresholds identified: 7 knots for resistance, 9 knots for trim divergence
- Performance benefits most pronounced under heavy-load condition with deeper bulb immersion
- Validated methodology applicable to high-speed fishing vessels operating up to $Fr = 0.59$

Numerical and Experimental Hydrodynamic Assessment of a Dihedral Bulbous Bow Retrofit for a Semi-Planing Fishing Vessel⋆

H. R. Díaz-Ojeda[a,*], Yifu Zhang[b,c,*], Tahsin Tezdogan[b] and Francisco Pérez Arribas[d]

[a]Universidad de Las Palmas de Gran Canaria, Campus de Tafira, Las Palmas de Gran Canaria, 35017, España
[b]Maritime Engineering University of Southampton Boldrewood Campus Southampton SO16 7QF Hampshire United Kingdom
[c]High Performance Computing (HPC) Team, University of Southampton, Highfield Campus, Southampton, SO17 1BJ, Hampshire, UK
[d]Universidad Politécnica de Madrid, Calle Ramiro de Maeztu 7, Madrid, 28040, España

ARTICLE INFO

Keywords:
Dihedral bulbous bow
Fast fishing vessel
Ship hydrodynamics evaluation
Ship power estimation
EFD CFD

Abstract

This study investigates the improvement in hydrodynamic performance achieved through the integration of a dihedral bulbous bow into a semi-planing fishing vessel, with particular emphasis on calm-water resistance and dynamic trim behavior. The results indicate a total resistance reduction of up to 28% under light-load condition and up to 32% under heavy-load condition.

A dihedral bulbous bow is a developable surface bulbous bow appendage that partially pierces the free surface rather than being fully submerged. Both experimental towing tank tests and numerical simulations using computational fluid dynamics (CFD) are conducted to evaluate the retrofit effectiveness. The vessel examined is a traditional artisanal longliner fishing boat, as classified by the Food and Agriculture Organization (FAO), operating at high speeds with Froude numbers approaching 0.5, significantly higher than conventional displacement-type fishing vessels.

The results emphasise the critical influence of dynamic lift forces on hull performance at elevated Froude numbers, where semi-planing behavior becomes dominant. Implementation of the dihedral bulbous bow demonstrates measurable improvements in hydrodynamic efficiency through favorable modifications to the wave pattern and pressure distribution around the hull. The combined effects of bow-generated lift, dynamic trim adjustment, and altered flow field contribute to reduced total resistance. Comparative analysis reveals distinct differences in the fluid dynamic behavior between the original hull and the retrofitted configuration, providing valuable insights for the design optimisation of high-speed fishing vessels.

1. Introduction

In naval architecture, the design and construction of a vessel requires careful consideration of various factors including stability, hydrodynamics, propulsion, and structural integrity. Among these, hydrodynamic performance is critically influenced by the vessel's intended operational profile, encompassing the ship's function, area of operation, and specific mission requirements.

Traditionally, ship design has relied on empirical knowledge supported in early design stages by statistical methods, such as those proposed by [8] and [7], or [13] specifically for bulbous bow design. However, in the case of fishing vessels—particularly artisanal ones—many have been built without rigorous hydrodynamic analysis, primarily due to economic constraints. These vessels are often commissioned by small shipowners who, even today, lack access to adequate financial resources to support the development of optimised designs or to evaluate alternatives tailored to their specific operational requirements. Consequently, designs are frequently based on existing vessels or derived from legacy hull forms, some of which may be decades old or developed for different service profiles. Furthermore, these vessels often undergo modifications throughout their service life to address evolving operational needs, typically without comprehensive experimental or numerical hydrodynamic assessment. This situation is compounded by the absence of systematic hull form updates over time.

Today, many hull forms remain in widespread use, including those published by FAO [6], which have received limited hydrodynamic evaluation or are based on relatively outdated design practices. These vessels are generally inefficient in terms of energy consumption, resulting in excessive fuel usage and increased environmental emissions compared to modern designs incorporating advanced propulsion systems or optimised hull forms [1]. This issue is particularly acute in developing regions where resources are scarce. However, similar challenges exist in developed countries [4], where ageing artisanal fleets operate with limited budgets for hydrodynamic studies and vessel improvements. This situation diminishes the sector's competitiveness, yet optimizing the performance of these vessels could yield substantial benefits including reduced fuel consumption, lower emissions, enhanced environmental sustainability, and decreased operational costs for fishermen.

Nevertheless, the solution does not lie in simply decommissioning existing vessels and replacing them with new construction, as the financial burden is often prohibitive—not only in developing regions but frequently in developed markets as well. Instead, retrofitting existing vessels emerges as a more economically viable alternative. The

⋆This document is the results of the research project funded by the Spanish Ministry of Ciencia e Innovación through grant PID2022-140481OB-I00.

hectorruben.diaz@ulpgc.es (H.R. Díaz-Ojeda); yifu.zhang@soton.ac.uk (Y. Zhang)
ORCID(s):

Table 1
Nomenclature of main hydrostatic and geometric parameters.

Symbol	Definition
LOA	Length Overall.
Lpp	Length between Perpendiculars.
Lwl	Length on Waterline.
BOA	Breadth Overall.
T	Draft.
DISv	Displacement Volume.
DISM	Displacement Mass.
S	Wetted Surface Area.
CDG	Center of Gravity.

critical question then becomes: how should these retrofits be most effectively implemented?

Effective retrofitting requires a comprehensive analysis of the vessel's current hydrodynamic performance, followed by targeted modifications aimed at reducing resistance and improving operational efficiency [15]. Crucially, these improvements must be achieved without significantly altering the vessel's principal characteristics, as many vessels are constrained by regulatory limits on gross and net tonnage and principal dimensions. Therefore, modifications must be carefully designed to remain within existing parameters.

One modification of particular interest is the incorporation of a bow bulb. Bulbous bows have become standard features in merchant ship design due to their proven effectiveness in reducing wave-making resistance at higher speeds. In contrast, many artisanal fishing vessels lack bulbous bows despite their potential benefits. Previous work by the authors explored the development of a dihedral bulbous bow shape for an artisanal vessel [16], demonstrating significant performance improvements at certain speeds [2] compared to the original hull without a bulbous bow.

Bow bulbs are effective within specific speed ranges [19], where they can substantially reduce wave-making resistance—the dominant resistance component at higher speeds [20]. However, fishing vessels present greater complexity than merchant ships. They often feature diverse length-to-beam ratios and operate under highly variable conditions, including shallow and deep waters, riverine navigation, and fluctuating speeds. For instance, they may travel slowly when departing port or during fishing operations, yet achieve higher speeds when transiting to or returning from fishing grounds. Consequently, it is essential to evaluate a broad range of speeds and loading conditions to determine the necessity and effectiveness of bulbous bow integration. The inverse problem—removing an existing bulbous bow—has also been investigated [3], demonstrating the complexity and variety of approaches applicable to the same hull form. These considerations are further complicated by the operational realities of artisanal fishing, where vessels often lack adequate onboard refrigeration, necessitating rapid return to port to preserve catch quality. These operational requirements, combined with complex hull forms and variable navigation conditions, underscore the importance of conducting vessel-specific hydrodynamic analyses. Ultimately, all considerations must align with the fisherman's primary objective: maximizing economic viability. In this context, retrofitting traditional fishing vessels—particularly through modifications such as bulbous bow addition—offers a promising pathway toward improving energy efficiency and reducing environmental impact. However, such interventions must be informed by detailed hydrodynamic studies that account for each vessel's unique operational and structural characteristics.

Another issue to be taken into account once the bulbous implementation is reached is that fishing vessels carrying sufficiently large payloads, which inherently limit their attainable operating speeds together with the absence of fine hydrodynamic hull lines, are typically characterized by displacement hull forms. Nevertheless, a comparative assessment between semi-planing and displacement hulls is required in order to develop a clearer understanding of the hydrodynamic relevance of incorporating a bulbous bow into a fishing vessel hull that operates at higher Froude numbers, since semi-planing configurations are also encountered in practical applications. Planing and semi-planning hulls achieve resistance reduction primarily through the generation of hydrodynamic lift. As vessel speed increases, this lift progressively raises a substantial portion of the hull out of the water, leading to a marked reduction in wetted surface area and, consequently, to a different distribution of wave generation. Under these conditions, the vessel weight is largely supported by dynamic pressure, while hydrostatic buoyancy becomes a secondary contributor. This implies a different design perspective for the bulbous bow when compared with conventional merchant vessels or generic displacement hull forms. By contrast, displacement hulls equipped with a bulbous bow remain fully supported by hydrostatic buoyancy throughout their entire operational speed range. For these hull forms, resistance reduction is mainly obtained through wave-interference effects. The bulbous bow generates a secondary wave system that partially cancels the primary bow wave produced by the forward hull geometry, thereby reducing wave-making resistance. This mechanism is effective only within a limited speed interval and is typically optimized for low to moderate Froude numbers, approximately in the range Fr $\approx$ 0.15–0.30.

These conditions closely correspond to the cruising speeds of many trawlers and long-range fishing vessels, for which the incorporation of a bulbous bow can yield measurable improvements in propulsive efficiency and fuel economy.

Building upon these considerations, this study presents a combined numerical and experimental investigation of an artisanal planing fishing vessel at model scale in calm water conditions. The analysis evaluates the vessel's resistance characteristics and other hydrodynamic properties, particularly dynamic trim behavior. The primary objective is to assess the performance improvements achievable through implementation of a retrofit-capable dihedral bulbous bow—specifically, a bulb that can be installed on existing vessels without requiring extensive structural modifications. Similar optimisation objectives have been pursued through alternative approaches in other studies [10], [22], [18].

Although fishing vessels typically operate at moderate Froude numbers, the vessel examined in this study is capable of reaching significantly higher speeds, with Froude numbers approaching 0.5. This places it within a hydrodynamic regime where wave-making resistance becomes a substantial component of total resistance, thereby enhancing the potential effectiveness of a bulbous bow intervention. The present study focuses on a vessel with a semi-planing hull form, a vessel type that has been extensively investigated [21]. However, since planing vessels primarily rely on dynamic lift forces rather than buoyancy—unlike merchant ships or displacement vessels that are predominantly affected by wave-making resistance—studies investigating the hydrodynamics of planing hulls with bulbous bows are uncommon. Only limited research has addressed this topic, specifically examining bulbous bow integration in high-speed vessels [9], [14]. Therefore, this study provides a novel contribution by examining the hydrodynamic behavior of a high-speed semi-planing vessel equipped with a bulbous bow, including its influence during planing conditions.

The investigations are conducted on an actual hull form provided by the FAO of the United Nations [5] and aim to provide insights that can be extrapolated to similar hull forms, given the limited availability of hydrodynamic literature focused on fishing vessels—particularly those with the specific operational characteristics examined here. This work therefore aims to contribute to the scientific understanding of such vessels and to serve as a practical reference for naval architects, marine engineers, and designers involved in developing and optimizing fishing vessel designs.

Finally, the study addresses several key research questions: What are the quantifiable advantages of implementing a retrofit bulbous bow for this class of hulls? At what operational conditions—or within what range of speeds and loadings—do these advantages become significant? To address these questions, the vessel is analysed across a wide range of speeds and two principal loading conditions to comprehensively evaluate hydrodynamic forces under various operational scenarios.

2. Vessel characteristics

This section describes the baseline vessel geometry and its modified configuration examined in the present study. The hull form originates from design plans published by the FAO of the United Nations, which has promoted the development of artisanal fishing vessel designs for several decades to support developing nations and their fishing communities in securing sustainable protein sources.

The FAO provides vessel design plans freely for educational, research, and professional applications through its official repository. These designs share a common limitation: being derived from traditional hull forms developed decades ago, they lack comprehensive hydrodynamic optimisation and are not adapted to contemporary operational and environmental requirements. Hydrodynamic refinement of these legacy designs could substantially benefit local fishing communities through improved fuel efficiency, reduced operational costs, and enhanced environmental sustainability.

The present work focuses on a longliner fishing vessel design representative of vessels operating in the Grenada region of the Eastern Caribbean. Grenadian longliners typically range from 9 m to 18 m in length overall (LOA) and comprise either traditional round-bilge wooden hulls or imported fibre-reinforced plastic (FRP) hard-chine hulls originally designed as sports fishing vessels and subsequently adapted for commercial longlining operations. The typical general arrangement includes a forward cabin below the main deck, wheelhouse located just forward of midships, insulated fish hold at midships, and a spacious aft working deck. The machinery space is positioned beneath the aft deck, followed by an aft lazarette housing the rudder stock. These vessels operate in both Caribbean Sea and Atlantic Ocean waters, with typical fishing voyages lasting 10 to 14 days.

Fuel represents a substantial proportion of operational expenditure in Caribbean small-scale fisheries, rendering fuel consumption reduction critically important to vessel economics and fisher livelihoods. The objective of this study is to quantify potential improvements in hydrodynamic efficiency through hull form modification, specifically through the addition of a dihedral bulbous bow, thereby reducing fuel consumption and operational costs. The improved designs developed through this research are intended for adoption by local fishing communities and for educational purposes in maritime training institutions.

From an economic perspective, retrofitting existing vessels through targeted modifications is significantly more cost-effective than new construction—a critical consideration in resource-constrained developing regions. The selection and design of the bulbous bow configuration builds upon the authors' prior research [16], while accounting for the construction capabilities and technological limitations typical of small shipyards in developing nations. Sophisticated hull modifications requiring advanced manufacturing techniques would be impractical and economically unviable in these contexts.

(a) Original (without bulbous bow)

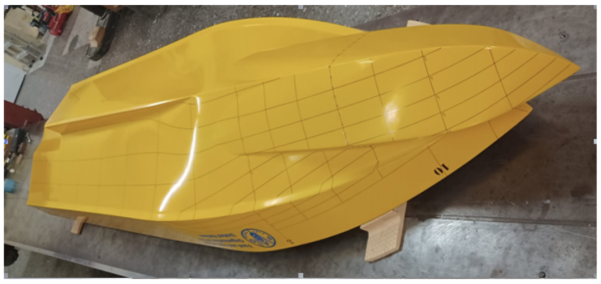

(b) Bulbous (with bulbous bow)

Figure 1: Comparison of FAO 3 models at model scale $\lambda = 6$.

Table 2
Comparison of main dimensions and hydrostatic data for FAO 3 no bulbous Heavy and Light ship - model scale (scale 1:6).

Ship Name **Scale**	FAO 3 Heavy 6		FAO 3 Light 6	
	Ship	Model	Ship	Model
LOA	15.2 m	2.533	15.2 m	2.533
Lpp	13.412 m	2.235	13.412 m	2.235
Lwl	13.412 m	2.235	13.189 m	2.198
BOA	4.439 m	0.740	4.439 m	0.740
T	1.118 m	0.186	0.914 m	0.152
DISv	20.321 m^3	0.094	11.264 m^3	0.052
DISM	20848 kg	96.52	11555 kg	52.19
S	59.174 m^2	1.64	51.372 m^2	1.43

Table 3
Comparison of main dimensions and hydrostatic data for FAO 3 with bulbous Heavy and Light ship - model scale (scale 1:6).

Ship Name **Scale**	FAO 3 Bulbous Heavy 6		FAO 3 Bulbous Light 6	
	Ship	Model	Ship	Model
LOA	15.2 m	2.533	15.2 m	2.533
Lpp	13.412 m	2.235	13.412 m	2.235
Lwl	15.023 m	2.504	14.863 m	2.477
BOA	4.439 m	0.740	4.439 m	0.740
T	1.118 m	0.186	0.914 m	0.152
DISv	21.948 m^3	0.102	12.345 m^3	0.057
DISM	22516 kg	101.70	12664 kg	57.20
S	63.431 m^2	1.762	54.93 m^2	1.53

Figure 1 presents both configurations examined in this study at model scale: the baseline hull without bulbous bow (representing the as-built vessel currently in service) and the modified hull incorporating the developable dihedral bulbous bow retrofit. Both configurations were subjected to experimental towing tank testing and numerical CFD analysis.

A geometric scaling ratio of $\lambda = 6.0$ was selected for the experimental programme, corresponding to Froude scaling between the model and full-scale vessel. The principal particulars and hydrostatic properties for both hull configurations are presented in Table **??** for the baseline hull and Table 3 for the modified hull with bulbous bow. Two loading conditions were examined to represent the operational envelope: a heavy-load departure condition corresponding to maximum displacement and deeper draught when departing port with full fuel and provisions, and a light-load arrival condition representing reduced displacement and shallower draught upon return to port after fuel consumption and cargo discharge. These loading conditions bound the typical operational draught range and capture the hydrodynamic behaviour across the vessel's service profile. All symbols, nomenclature, and units are defined in the Nomenclature section.

Figure 2 presents the lines plan of the baseline FAO hull, showing the body plan, half-breadth plan, and sheer profile. This geometry serves as the reference configuration for subsequent modification and serves as the basis for bulbous bow integration.

3. Methodology

3.1. Experimental set up

This investigation employs a combined experimental and numerical approach to assess the hydrodynamic performance of the baseline and modified hull configurations. Experimental tests were conducted first to establish benchmark resistance and dynamic trim data, followed by CFD simulations to validate the experimental results and provide detailed flow field analysis. This complementary methodology enables verification of numerical predictions against physical measurements while providing insight into the underlying flow physics that cannot be readily obtained through experimentation alone.

The validated CFD framework subsequently enables parametric investigation of hull modifications and design variations without the time and cost constraints of physical model testing. Following initial validation against experimental data, the numerical approach can be applied to evaluate additional design configurations or operational scenarios with confidence in predictive accuracy.

All investigations were conducted in calm water conditions without consideration of wave excitation, wind loading, or other environmental effects. This approach isolates the resistance and dynamic trim characteristics attributable solely to hull geometry and hydrodynamic performance.

The experimental campaign was conducted in the towing tank of the Naval Architecture Department at the Technical University of Madrid (Universidad Politécnica de Madrid),

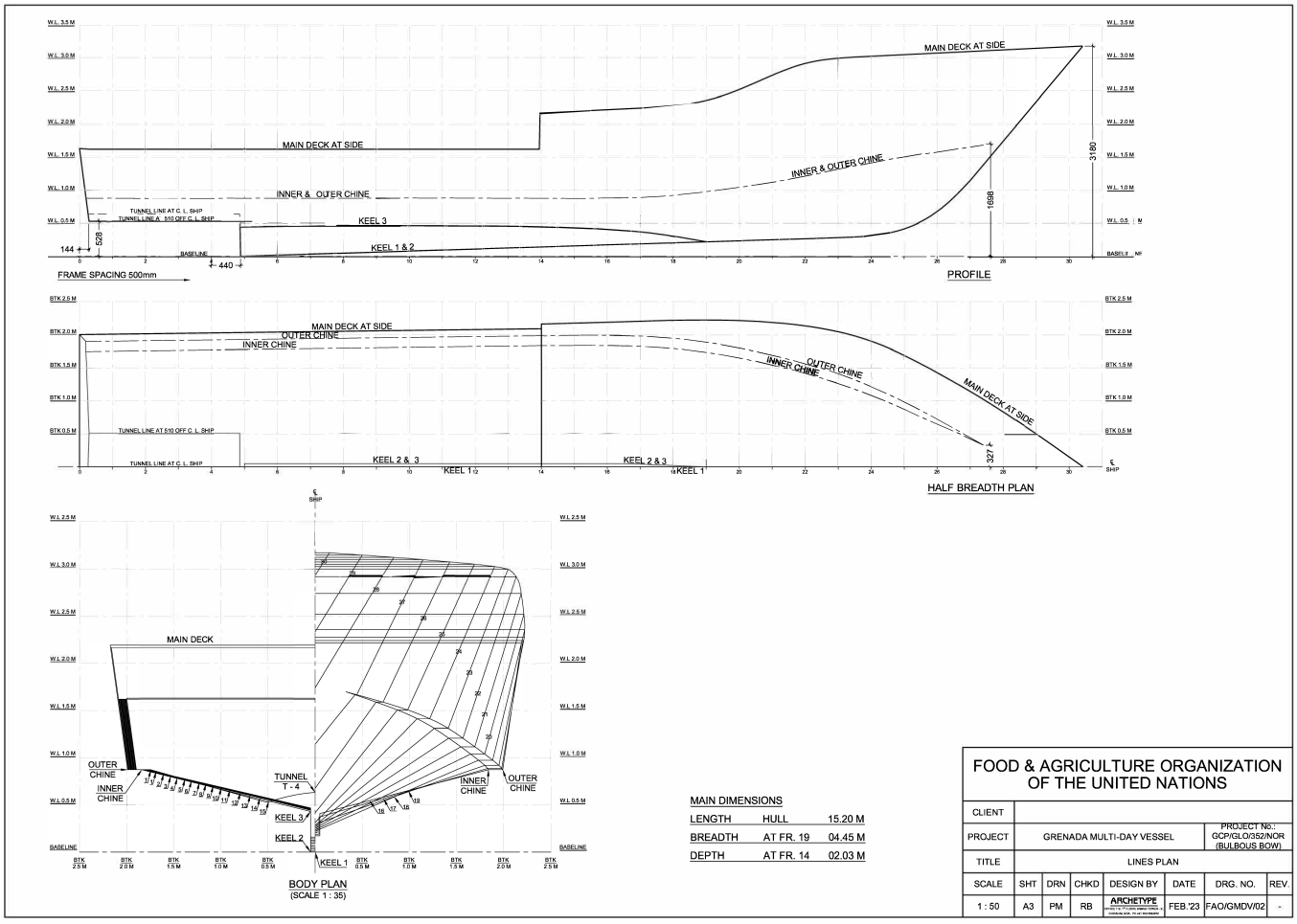

Figure 2: Original FAO hull lines [5], [6]. The figure shows the profile, half-breadth, and body plan used as the baseline geometry for the study.

Spain. The facility measures 100 m in length, 3.8 m in width, and 2.2 m in depth. The model scale and test speeds were selected to ensure negligible blockage and shallow-water effects, with depth Froude numbers maintained well below critical values.

The experimental procedures followed established ITTC (International Towing Tank Conference) guidelines and methodologies consistent with the authors' previous investigations [16], [2], [3] such as [17], [11] or [12]. Each test run commenced with the towing carriage accelerating from rest to the target velocity, replicating the transient acceleration phase employed in the numerical simulations. During the acceleration phase, a mechanical clamp restrained the model to prevent overloading the force transducer. Once steady velocity was achieved, the clamp was released and the model was constrained by a guidance system permitting three degrees of freedom: surge (longitudinal translation), heave (vertical translation), and pitch (rotation about the transverse axis). The remaining three degrees of freedom (sway, roll, and yaw) were restrained. Dynamic sinkage and trim angle were measured using two laser displacement sensors positioned at the forward and aft perpendiculars.

Towing resistance was measured using a calibrated strain-gauge load cell (Schenck Z6 bending beam dynamometer) mounted to the towing carriage through a pulley-spring-cable system. The load cell sampled at 10 Hz and measured the force component aligned with the towing direction. The dynamometer was calibrated over a range exceeding 4 kg, corresponding to the maximum anticipated model resistance. Water temperature was monitored throughout testing (16 °C)) to enable accurate kinematic viscosity determination for Reynolds number calculations and full-scale extrapolation following ITTC procedures.

As illustrated in Figure 3, two loading conditions were examined: a heavy-load condition representing departure with full fuel and provisions, and a light-load condition representing arrival after fuel consumption. Tests were conducted over a speed range from 2 knots to 14 knots at full scale (equivalent to Froude numbers from 0.08 to 0.59), with particular emphasis on operationally significant speeds identified by vessel operators: 6 knots (displacement regime),

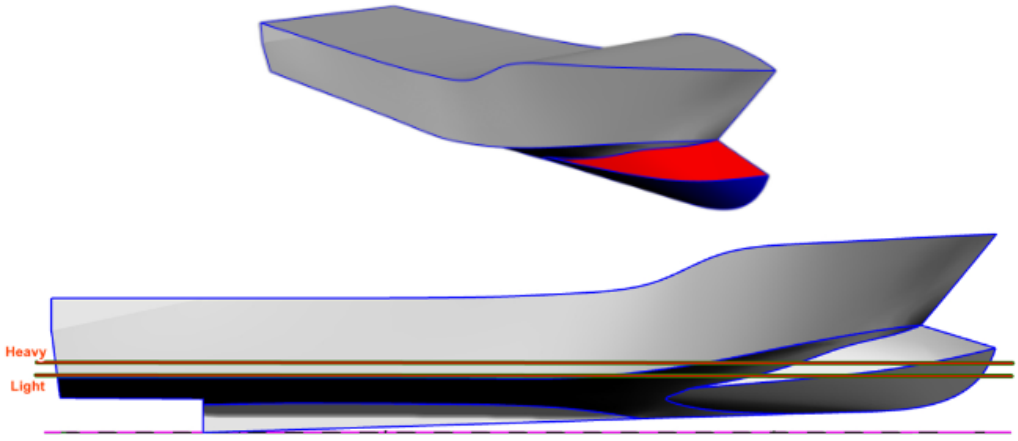

Figure 3: 3D model of the hull with bulbous bow and loading conditions.

8 knots (transition regime), and 11 knots (semi-planing regime). The maximum test speed corresponds to Fr = 0.59, placing the vessel firmly within the planing regime where dynamic lift forces dominate the vertical force balance.

3.2. Numerical set up

The numerical simulations were performed using the open-source finite volume CFD solver OpenFOAM v12. The computational framework extends the methodologies established in the authors' previous work [16], [2], [3], where comprehensive descriptions of the numerical configuration, boundary conditions, and solution procedures are provided.

Turbulence closure was achieved using Reynolds-averaged Navier–Stokes (RANS) equations coupled with the k–ω shear stress transport (SST) turbulence model. This two-equation eddy viscosity model was selected for its demonstrated accuracy in maritime hydrodynamics applications, particularly in resolving boundary layer flows under adverse pressure gradients and capturing flow separation phenomena. The model transitions smoothly between the k–ω formulation near walls and a k–ϵ behaviour in the free stream, providing robust predictions across the full boundary layer thickness.

Pressure–velocity coupling was treated using the PIMPLE algorithm, a hybrid procedure combining SIMPLE (Semi-Implicit Method for Pressure-Linked Equations) and PISO (Pressure-Implicit with Splitting of Operators) approaches. This iterative scheme enables larger time steps while maintaining solution stability and accuracy. The free surface between air and water was captured using the volume of fluid (VOF) method with interface compression to maintain sharp phase boundaries.

3.3. Computational Domain and Mesh Generation

The computational domain exploits the longitudinal symmetry plane of the hull, modelling only the starboard half to reduce computational expense. Predicted forces and moments were subsequently doubled to obtain total values for the complete hull.

Domain extents were established following best practices for maritime CFD to minimize boundary influence on the solution. The inlet boundary was positioned three ship lengths ($3L_{PP}$) upstream of the forward perpendicular, whilst the outlet was located eight ship lengths ($8L_{PP}$) downstream of the aft perpendicular. Lateral and bottom boundaries were positioned at three ship lengths ($3L_{PP}$) from the hull centreline and baseline, respectively. The top boundary was located at $1.5L_{PP}$ above the calm waterline. These domain dimensions have been validated in prior work [2] and are consistent with ITTC recommendations for resistance prediction.

The computational mesh employed a hierarchical refinement strategy. A baseline hexahedral grid was generated throughout the domain, with successive refinement regions concentrating cells near the hull surface and free surface interface. The refinement methodology follows the approach established in previous publications [2], incorporating four nested refinement zones (R1 through R4) with cell dimensions halved at each level. This systematic refinement ensures adequate resolution of velocity and pressure gradients in the boundary layer whilst maintaining computational efficiency in far-field regions.

Additional mesh refinement was applied in the vicinity of the free surface to accurately resolve wave generation, propagation, and breaking phenomena. The free surface zone extended from $0.5L_{PP}$ forward to $1.5L_{PP}$ aft of the hull, with vertical extent from one wave height below to one wave height above the nominal waterline. This region employed anisotropic cells with fine vertical spacing to capture the air-water interface and wave profile accurately. The mesh topology is illustrated in Figure 4.

The final mesh comprised approximately 7 million cells (mesh 1 4) , representing a balance between solution accuracy and computational cost. Detailed mesh independence studies, verification analyses, and convergence assessments have been conducted in previous investigations [2], [16] using identical meshing strategies.

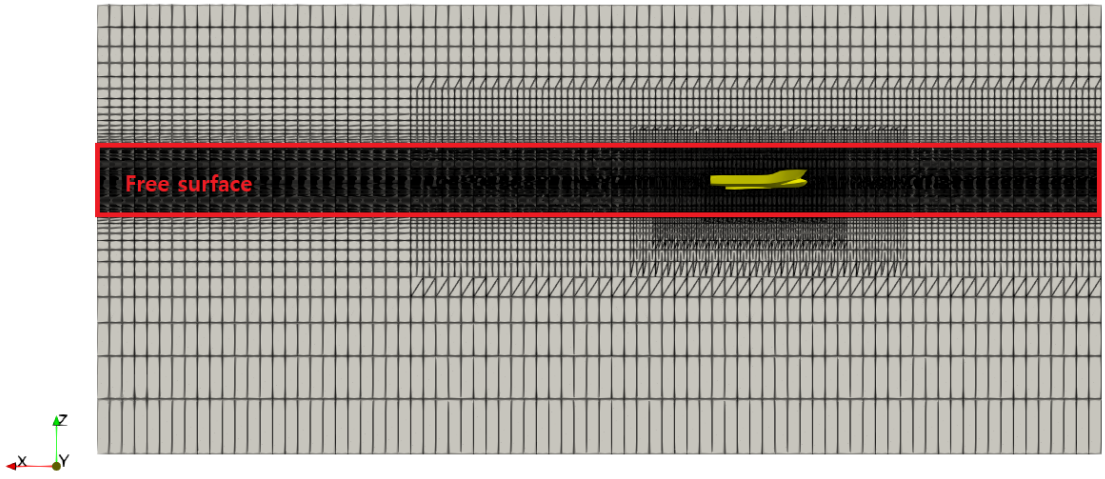

(a) Front view showing mesh refinement zones

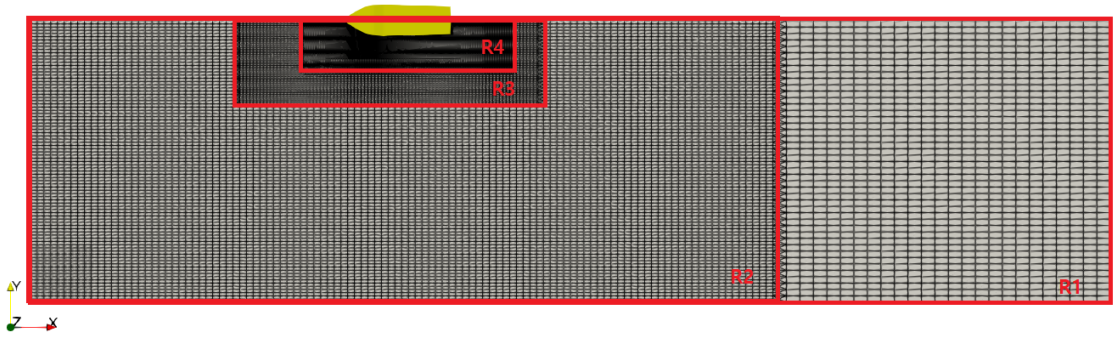

(b) Top view showing free surface refinement

Figure 4: Schematic representation of the mesh and its refinement for the computational domain.

The strategy adopted to carry out the computational fluid dynamics (CFD) studies was based on the previously cited works, from which a systematic mesh and time-step independence analysis was performed 4. Several mesh configurations were evaluated, with particular emphasis on achieving an adequate resolution of the air–water interface and an accurate discretization of the hull surface. Meshes with a total number of cells ranging from approximately $5-6\times10^6$ up to 8.2×10^6 were analyzed. The results show that the total drag force remains essentially unchanged when varying the mesh density, indicating a low sensitivity of this quantity to further mesh refinement. This behavior is mainly attributed to the high quality of the meshing applied to both the hull surface and the free surface, such that beyond a certain threshold, increasing the number of cells does not lead to a significant improvement in the numerical results.

A similar sensitivity analysis was conducted for the time step. Several time-step values were tested and are summarized in 4, including constant time steps of 5×10^{-4} s and 1×10^{-3} s, as well as a variable time-step approach in which a maximum Courant number was imposed. In all cases, the variation in the total resistance was found to be negligible, with very low associated errors, confirming that the selected time-step sizes are numerically acceptable. The convergence of the numerical setup is further verified by the consistency of the results when both the number of cells and the time step are varied.

This conclusion is additionally supported by the comparison with experimental data, which are presented in the following subsections and show excellent agreement with the numerically obtained values. Finally, for the simulations presented in this work, a variable time-step scheme was selected, as it significantly accelerates the convergence towards the final solution and reduces the overall computational cost. In particular, it was observed that the use of a larger time step, such as 1×10^{-3} s, provides results equivalent to those obtained with smaller time steps, while requiring substantially shorter computational times.

4. Results and Discussion

This section presents the experimental and numerical results obtained for both hull configurations across the investigated speed and loading condition matrix. The presentation follows a structured approach: first, validation of the CFD methodology against experimental measurements is demonstrated through comparison of resistance, trim, and wave pattern data; second, detailed analysis of hydrodynamic forces (resistance components and lift) is provided; third,

Table 4
Resultant force for different mesh resolutions and time-step sizes at $V = 1.68$ m/s.

Cells	Mesh	Time step (s)	Resultant force (N)
6775917	Mesh 1	0.0005	33.37
6775917	Mesh 1	0.0010	33.40
6775917	Mesh 1	Variable	32.70
5973176	Mesh 2	0.0005	33.06
5973176	Mesh 2	0.0010	33.03
5973176	Mesh 2	Variable	33.40
8155042	Mesh 3	0.0005	33.17
8155042	Mesh 3	0.0010	33.18
8155042	Mesh 3	Variable	33.28

dynamic trim behaviour is examined; and finally, experimental flow visualisation results are discussed to elucidate the physical mechanisms underlying the observed performance differences.

The validation demonstrates sufficiently low prediction errors to establish confidence in the CFD methodology as a reliable tool for performance assessment and for providing detailed flow field information that complements the experimental measurements. Following validation, comparative analysis between the baseline hull and the dihedral bulbous bow configuration is presented, with particular emphasis on identifying the operational regime where retrofit benefits become significant. Throughout this section, the modified configuration is referred to as the "dihedral bulbous bow" in reference to its geometric characteristics as described in [16].

Vertical force predictions are also presented, as these loads govern the vessel's dynamic trim equilibrium and emergence behaviour—phenomena of critical importance in semi-planing hulls where hydrodynamic lift becomes a substantial component of the vertical force balance.

4.1. Validation and Verification

Figure 5 presents comparative visualisations of the free surface elevation and wave pattern around both hull configurations at representative speeds. These comparisons demonstrate the CFD methodology's capability to reproduce the complex wave-making phenomena observed experimentally, including the bow wave system, shoulder wave, and transom stern wave. The free surface predictions provide insight into the pressure distribution along the hull and wave-generation mechanisms that are difficult to quantify experimentally but readily accessible through numerical simulation.

The figures reveal qualitative agreement between EFD and CFD wave patterns, with alternating wave crests and troughs appearing at corresponding longitudinal stations. These wave elevation profiles provide valuable design information, as regions of elevated free surface correspond to zones of high pressure where wave-making resistance is generated. The wavelength and amplitude of these disturbances are functions of Froude number and hull geometry, and their accurate prediction validates the numerical approach for subsequent parametric investigations.

Comparison between the baseline and dihedral bulbous bow configurations reveals distinctly different bow wave characteristics, indicating altered pressure distributions and wave interference mechanisms. These differences in wave-making behaviour translate directly to variations in wave-making resistance—a component that dominates total resistance at higher speeds. Validation is presented for speeds of 6 and 8 knots under both loading conditions, representing the displacement and early transitional speed regimes. Additionally, the CFD results clearly capture the transom stern wave and its modification by the presence of the bulbous bow, providing insight into the aft pressure recovery region.

Quantitative validation of resistance prediction is presented in Figures 6a and 6b for the light-load and heavy-load conditions, respectively. For both loading conditions, the mean prediction error remains below 6%, with only one test point exceeding 3% deviation. At Froude numbers below 0.27, experimental and numerical resistance values are nearly identical. Although these low-speed resistance values contribute minimally to installed power requirements, they provide valuable data for determination of the form factor (1+k) required for full-scale extrapolation via the ITTC'78 method, and confirm CFD accuracy across the complete speed range including the displacement regime.

Above Fr = 0.27, total resistance increases rapidly due to the growing contribution of wave-making resistance, yet the CFD predictions accurately reproduce the experimental trend with minimal error up to 12 knots (Fr = 0.54). At this Froude number, the vessel operates in the transitional regime approaching semi-planing conditions, where hull emergence and dynamic lift become significant. The heavy-load condition exhibits a similar resistance characteristic but with higher absolute values due to increased wetted surface area and deeper wave-making. The critical transition point occurs near 5–6 knots at full scale, beyond which resistance rises sharply, emphasising the substantial power penalty associated with high-speed operation at elevated displacement.

Dynamic trim validation is presented in Figures 7a and 7b for the light and heavy-load conditions, respectively. Both hull configurations (baseline and dihedral bulbous bow) are shown, yielding four validation cases in total. In all cases, the CFD predictions exhibit close agreement with experimental measurements across the speed range, with deviations typically below 0.5° in trim angle. This agreement confirms the capability of the RANS-VOF approach to predict not only resistance but also the dynamic equilibrium trim position resulting from the balance of longitudinal forces and moments.

For the light-load condition with the baseline hull, trim remains negligible (below 0.5°) up to approximately 8 knots, beyond which it increases rapidly due to the aft shift in the centre of pressure as hydrodynamic lift develops. In contrast, the dihedral bulbous bow configuration exhibits negligible trim up to 5 knots, followed by a more gradual linear increase between 5 and 9 knots, transitioning to exponential growth

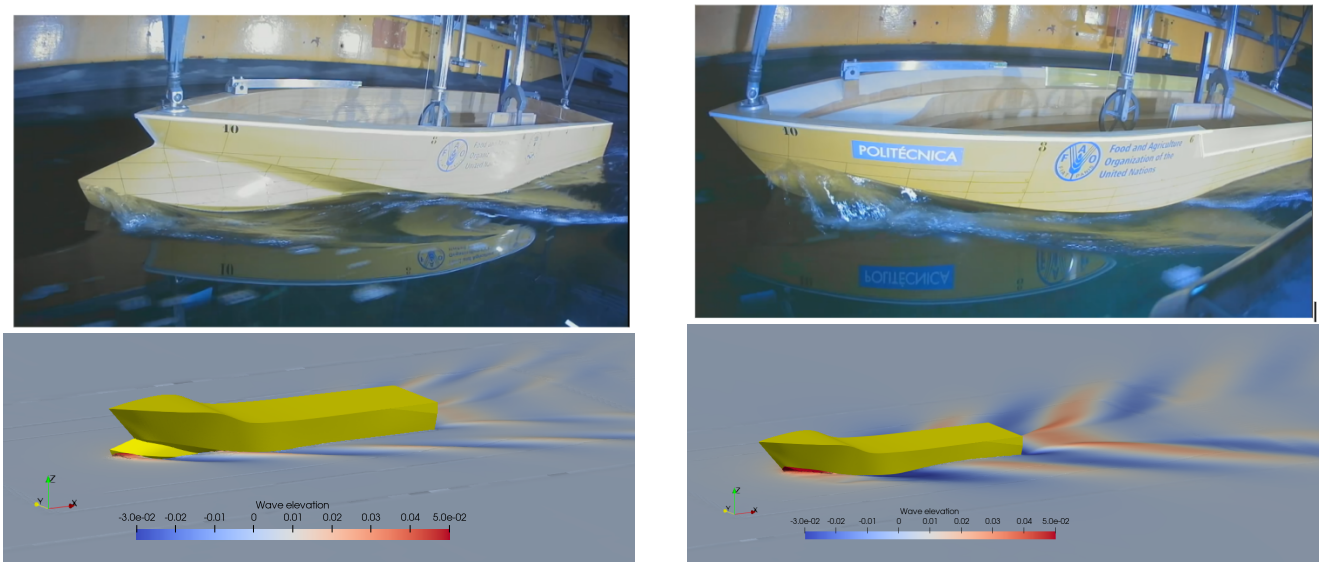

(a) 6 knots **(b)** 8 knots

Figure 5: Comparison between experimental and numerical wave patterns at 6 knots (a) and 8 knots (b) for hulls with and without bulbous bow under light-load condition. Top: experimental results; bottom: numerical (CFD) predictions.

beyond 9 knots. This behaviour indicates that the bulbous bow alters the longitudinal pressure distribution and centre of pressure location, affecting trim equilibrium at moderate speeds.

Under heavy-load condition, the baseline hull again maintains negligible trim up to 8 knots, with exponential growth commencing beyond 9 knots. When the dihedral bulbous bow is incorporated, trim remains negligible up to 5 knots. A localised perturbation is observed near 7 knots, where trim increases briefly before returning to near-zero values—likely associated with the transition between displacement and semi-planing flow regimes. Beyond 9 knots, trim increases exponentially, though consistently remaining below the baseline hull values at equivalent speeds.

4.2. Resistance Analysis and Force Decomposition

Figure 8a presents the total resistance for both hull configurations under light-load conditions. For clarity, only CFD predictions are shown, as validation has already demonstrated their accuracy. Up to approximately 7 knots, where the resistance curve transitions from linear to exponential growth, the two configurations exhibit nearly identical resistance values. In some cases, the dihedral bulbous bow shows marginally lower resistance, whilst at other speeds it is slightly higher—differences that fall within the uncertainty bounds and indicate no consistent benefit at low Froude numbers.

Beyond 7–8 knots, the dihedral bulbous bow configuration consistently demonstrates lower resistance. At 8 knots, resistance is reduced by approximately 3% relative to the baseline hull, and this benefit increases progressively with speed. The maximum resistance reduction of 28% occurs at 11 knots, representing the largest performance divergence between configurations observed in this study. To investigate whether this trend continues at higher speeds, additional simulations were conducted at 13 and 14 knots. Results indicate that the resistance reduction persists but diminishes slightly at these elevated speeds, yielding a 19% reduction at 14 knots (Fr = 0.59)—a speed approaching the practical operational limit for this vessel type.

Figure 8b presents the corresponding comparison for heavy-load condition. A similar trend is observed, with nearly identical resistance values for both configurations up to 5–7 knots. The divergence becomes pronounced from 8 knots onwards, where the dihedral bulbous bow achieves a 16% resistance reduction—substantially greater than the 3% observed at the same speed under light-load condition. This indicates that the bulbous bow benefit is more pronounced at higher displacement, likely due to the increased wave-making component and altered bow pressure field.

The maximum performance improvement under heavy-load condition occurs at 10 knots, where resistance is reduced by 32%—exceeding the 28% maximum reduction observed at 11 knots under light-load condition. This benefit persists at higher speeds, though gradually diminishing to 15% at 14 knots. Overall, the heavy-load condition demonstrates substantially greater resistance reduction compared to the light-load condition across the entire semi-planing speed regime, suggesting that the dihedral bulbous bow retrofit is particularly beneficial for vessels operating at high displacement-to-length ratios.

The CFD methodology enables decomposition of total resistance into pressure (form + wave-making) and viscous (frictional) components, facilitating identification of the physical mechanisms responsible for the observed resistance reduction. Figure 9 presents the pressure resistance

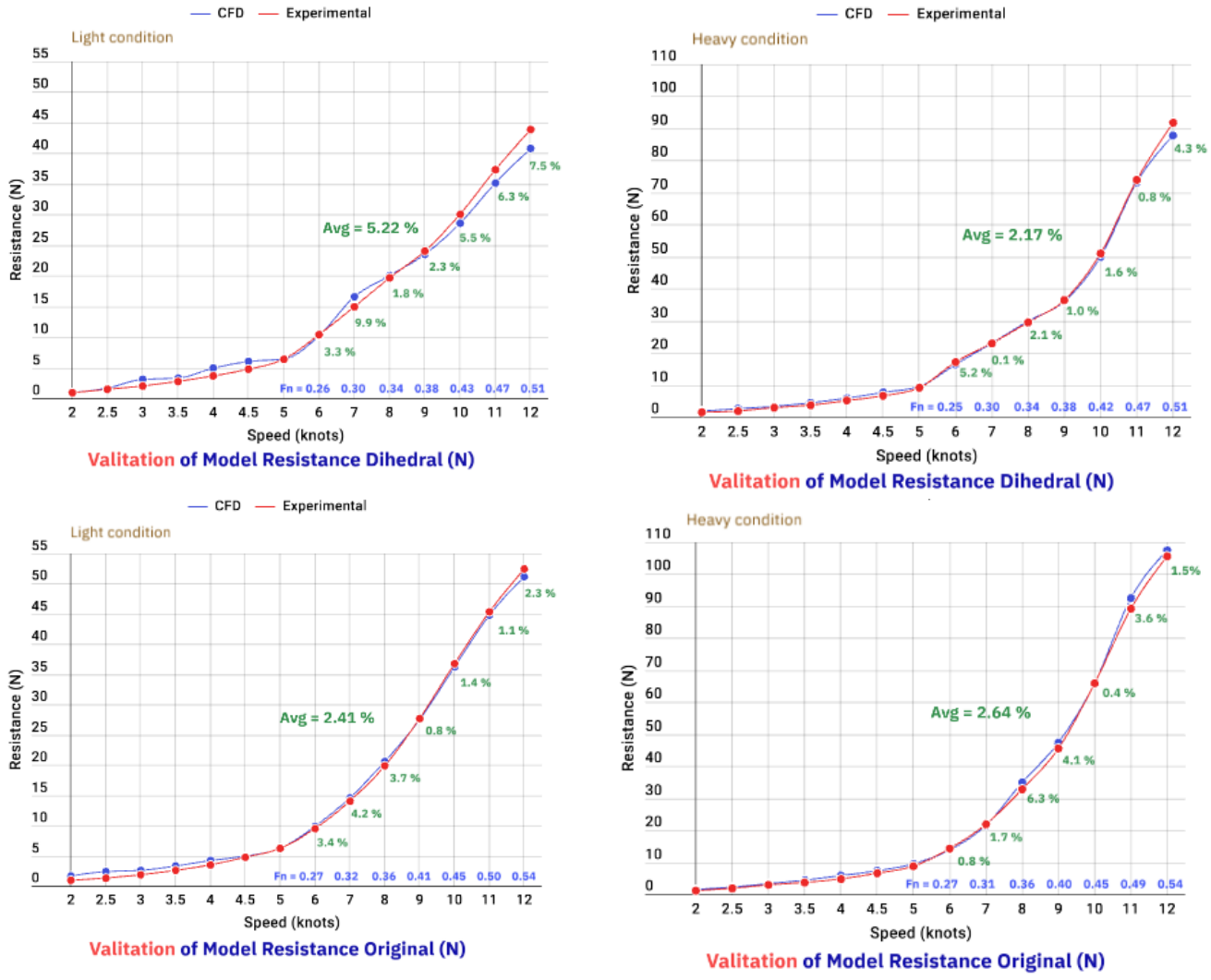

(a) Light-load condition

(b) Heavy-load condition

Figure 6: Validation of model resistance for both loading conditions: (a) light-load condition; (b) heavy-load condition. For each condition, top graph shows dihedral bulbous bow configuration and bottom graph shows original configuration.

component for both loading conditions. Under light-load condition, pressure resistance remains nearly identical for both configurations up to 7 knots, diverging thereafter with the dihedral bulbous bow exhibiting progressively lower values as speed increases. This behaviour confirms that the resistance benefit arises primarily from reduced wave-making and altered pressure distribution rather than from viscous effects.

For heavy-load condition, a similar trend is observed: pressure resistance values are nearly identical up to 7 knots and then gradually separate. The difference remains relatively constant until approximately 11 knots, beyond which it increases, with the dihedral bulbous bow configuration consistently exhibiting lower pressure resistance than the baseline hull. The critical speed of 7 knots corresponds to the transition between displacement and semi-planing regimes, where wave-making resistance begins to dominate and where bulbous bow interference effects become beneficial.

Figure 10 presents the viscous resistance component for both loading conditions. Under light-load condition, viscous resistance exhibits linear growth up to 5 knots, transitioning to steeper exponential growth beyond 6 knots as wetted surface area increases due to hull emergence and trim. Up to approximately 8 knots, viscous resistance remains nearly identical for both configurations, with only minor differences thereafter. Compared to pressure resistance, the viscous component contributes less to total resistance at higher speeds and is therefore less significant in determining overall bulbous bow effectiveness. Above 7 knots, pressure resistance becomes the dominant component governing performance differences.

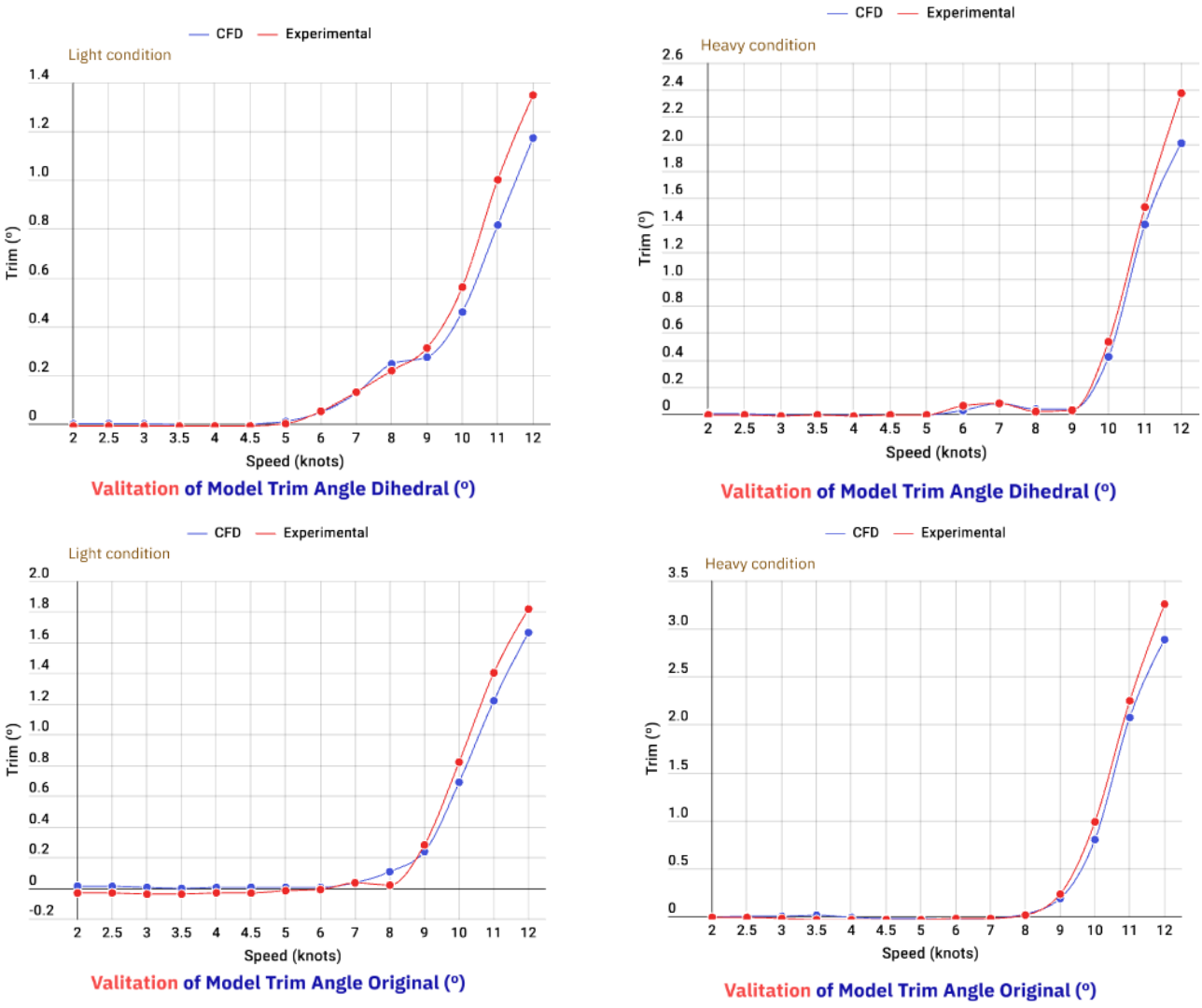

(a) Light-load condition

(b) Heavy-load condition

Figure 7: Validation of model trim angle for both loading conditions: (a) light-load condition; (b) heavy-load condition. For each condition, top graph shows dihedral bulbous bow configuration and bottom graph shows original configuration.

For heavy-load condition, the viscous resistance curves are nearly coincident across the entire speed range. Notably, incorporation of the dihedral bulbous bow does not increase viscous resistance despite the modest increase in wetted surface area; in fact, at 8, 9, and 10 knots, viscous resistance is marginally lower with the bulb, likely due to favourable trim reduction. This confirms that pressure resistance is the dominant mechanism responsible for the observed performance differences, with the critical transition speed of approximately 7 knots marking the onset of bulbous bow effectiveness.

4.3. Total resistance overview

To clarify the effects of added resistance, figure 11 is presented. These figures compare, on the one hand, the light condition and, on the other hand, the heavy condition, for cases with and without a bulbous bow. The analysis is performed by computing the difference in resistance between both configurations across the different velocities. The resulting percentage variation in resistance—representing either an improvement or a deterioration due to the bulbous bow—is shown on the left vertical axis (Y-axis). On the right axis, the absolute difference in total resistance at model scale, expressed in Newtons, is displayed.

This distinction is particularly relevant because, although in some cases a relatively high percentage difference in resistance can be observed—such as at 3 knots under light conditions—the corresponding absolute variation in resistance is practically negligible. This highlights the fact

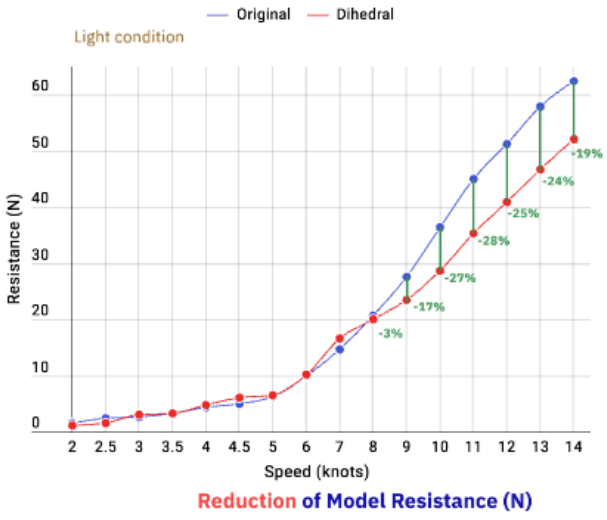

(a) Light-load condition

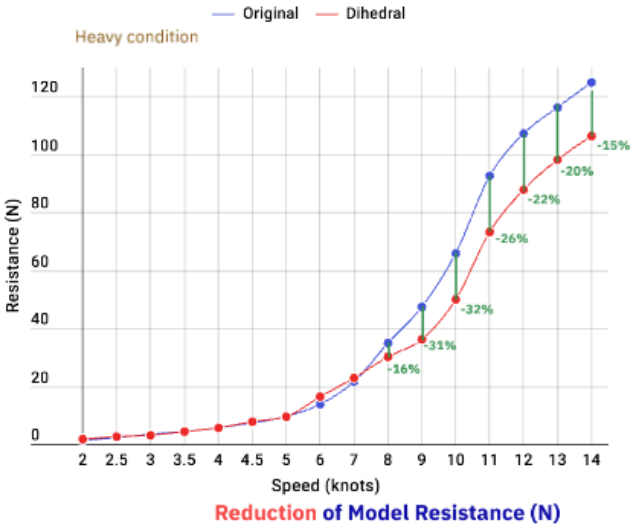

(b) Heavy-load condition

Figure 8: Total resistance comparison between original and dihedral bulbous bow configurations: (a) Light-load condition; (b) Heavy-load condition.

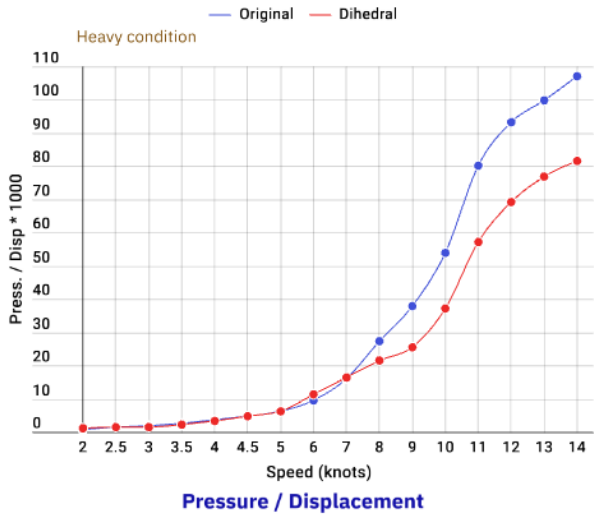

(a) heavy-load condition

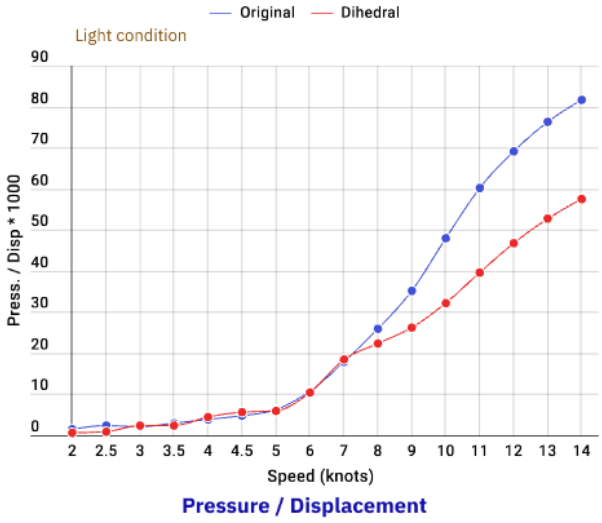

(b) light-load condition

Figure 9: Pressure resistance comparison for the original and dihedral bulbous bow configurations: (a) Heavy-load condition; (b) Light-load condition.

that percentage values and absolute resistance values are represented on different scales. The inclusion of both metrics allows the reader to verify that the percentage variations become truly meaningful mainly when significant resistance variations occur, which is approximately from 7.5 knots onward.

In the presented graphs, green and orange colors indicate cases in which no improvement is achieved through the implementation of the bulbous bow, whereas blue bar diagrams represent conditions where an improvement is obtained. The results show that the majority of the resistance reduction occurs at speeds of 9, 10, and 11 knots, under both light and heavy loading conditions. Furthermore, a notable increase in efficiency is observed when the resistance that contributes most significantly to the total resistance begins to grow.

For instance, under light conditions, from approximately 8 knots onward, the resistance increases in a nearly linear—almost exponential—manner up to a maximum value. These speed ranges coincide with the points at which the bulbous bow provides the highest efficiency gains. This

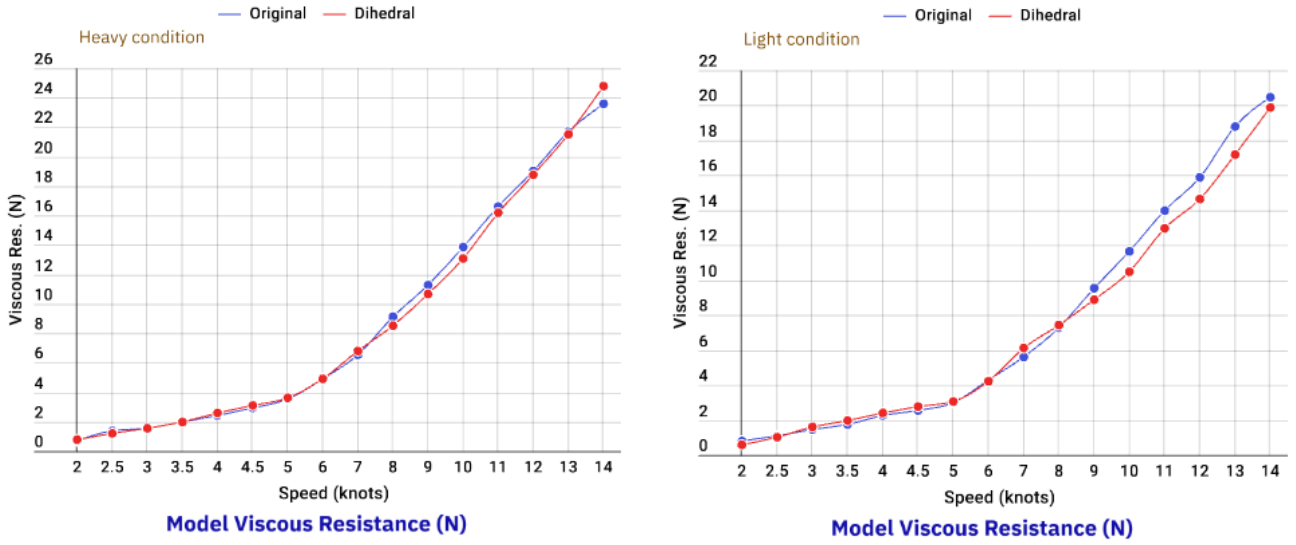

(a) Heavy-load condition

(b) Light-load condition

Figure 10: Viscous resistance comparison for the original and dihedral bulbous bow configurations: (a) heavy-load condition; (b) light-load condition.

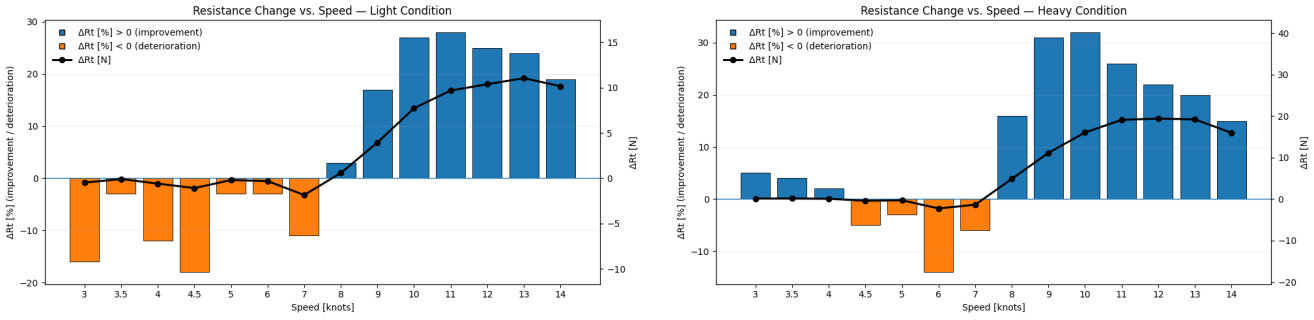

(a) Heavy-load condition

(b) Light-load condition

Figure 11: Resistance change versus speed under the light and heavy load condition. Bars show the percentage variation in total resistance (ΔR_t), where positive values indicate improvement and negative values indicate deterioration. The black curve shows the absolute difference in total resistance at model scale (N).

improvement remains consistent up to a speed of 14 knots, as also observed previously, making the implementation of the bulbous bow particularly attractive.

Although a deterioration in total resistance is observed at lower speeds—specifically below 8 knots for light conditions and between 7 and 8 knots for heavy conditions—these resistance values are sufficiently low that they do not result in a significant increase in fuel consumption, resistance-related costs, or associated emissions.

Analogously, 12 presents the comparison obtained when superimposing the light- and heavy-load conditions, in relation to the separate trends shown in 11. This combined view must be interpreted with caution, since the absolute resistance levels and the vessel response differ between loading conditions. Nevertheless, from a percentage-based perspective, it provides a clear indication of the speed ranges at which the bulbous bow is expected to perform more effectively under each condition.

The black curves (both solid and dashed) are included to represent the experimentally measured resistance differences for each case. The results indicate that, for the heavy-load condition, the bulbous bow yields a markedly higher benefit within the 8–10 kn range compared to the light-load condition. Conversely, beyond approximately 10–11 kn, the light-load condition exhibits a higher percentage improvement than the heavy-load case.

4.4. Vertical Force Analysis

An additional quantity accessible through CFD but not measured experimentally is the vertical hydrodynamic lift force. This force component determines the magnitude of dynamic lift supporting the vessel's weight and governs

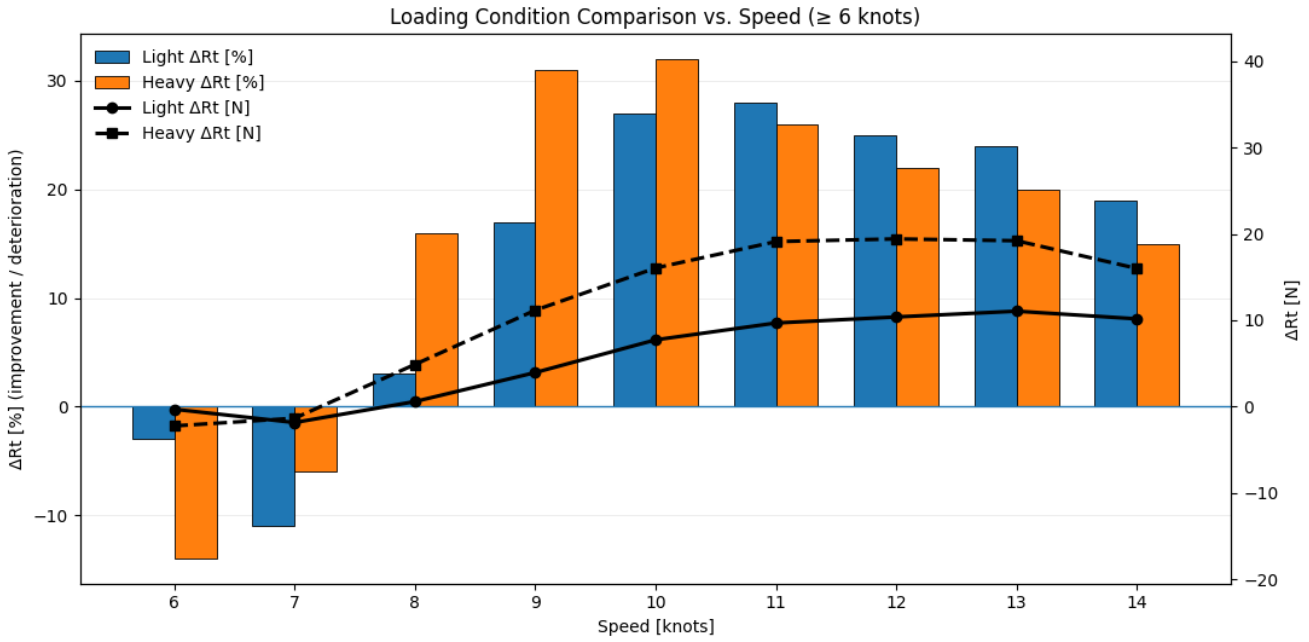

Figure 12: Comparison between light- and heavy-load conditions as a function of speed for velocities greater than or equal to 6 knots. Bars represent the percentage variation in total resistance (ΔR_t), where positive values indicate improvement and negative values indicate deterioration. Solid and dashed black curves show the absolute difference in total resistance at model scale (N) for light- and heavy-load conditions, respectively.

emergence, trim equilibrium, and the transition to planing conditions. Figure 13 presents the lift force for both loading conditions.

Under light-load condition, the dihedral bulbous bow configuration produces lower lift compared to the baseline hull across most of the speed range. Between 2 and 4.5 knots, lift remains nearly constant, then increases linearly up to 7 knots, followed by a sharp rise until 9 knots. At this speed, lift reaches a local maximum that persists nearly constant up to 12 knots before decreasing. Whilst the overall trend is qualitatively similar for both configurations, the baseline hull consistently generates higher lift forces. This difference suggests that the dihedral bulbous bow alters the bow pressure distribution in a manner that reduces vertical force generation whilst simultaneously reducing resistance—a favourable trade-off for vessels not requiring maximum dynamic lift.

Under heavy-load condition, the behaviour reverses: the dihedral bulbous bow configuration produces greater vertical lift force than the baseline hull. Lift remains nearly constant up to 5 knots, increases linearly until 7 knots, then rises sharply until 10 knots, where a pronounced peak occurs before declining. This maximum at 10 knots corresponds to Fr=0.42, near the threshold of fully-developed planing conditions. The baseline hull follows a broadly similar trend, with both configurations reaching maximum lift near 10–11 knots before decreasing at higher speeds—likely due to increased trim and altered angle of attack of the planing surfaces.

The reversal in relative lift between loading conditions suggests that the dihedral bulbous bow's influence on the pressure field is sensitive to displacement and trim. Under heavy-load condition, where the bulb is more deeply immersed and the bow wave is more pronounced, the bulb generates additional vertical force that aids in supporting the increased weight whilst simultaneously reducing wavemaking resistance.

4.5. Dynamic Trim Behaviour

Figure 14a presents the CFD-predicted trim angles for both hull configurations under light-load condition. Up to approximately 5–6 knots, trim remains negligible (below 0.5°). Between 6 and 9 knots, the dihedral bulbous bow configuration exhibits greater trim than the baseline hull, indicating an aft shift in the longitudinal centre of pressure. At 9 knots, a critical transition occurs and the trend reverses: beyond this speed, the dihedral bulbous bow consistently produces lower trim than the baseline hull. This trim reduction is operationally significant, as excessive bow-up trim adversely affects propeller immersion, increases appendage drag, reduces directional stability, and increases wetted surface area due to the emergence of aft hull sections.

For heavy-load condition (Figure 14b), trim remains negligible up to approximately 8 knots. From 9 knots onwards, trim increases dramatically, reaching nearly 13° at 12 knots for the baseline hull—an extreme attitude that would severely compromise operational performance in a real vessel. At all speeds above 9 knots, the dihedral bulbous bow configuration exhibits substantially lower trim compared to the baseline hull. The critical speed of 9 knots represents the

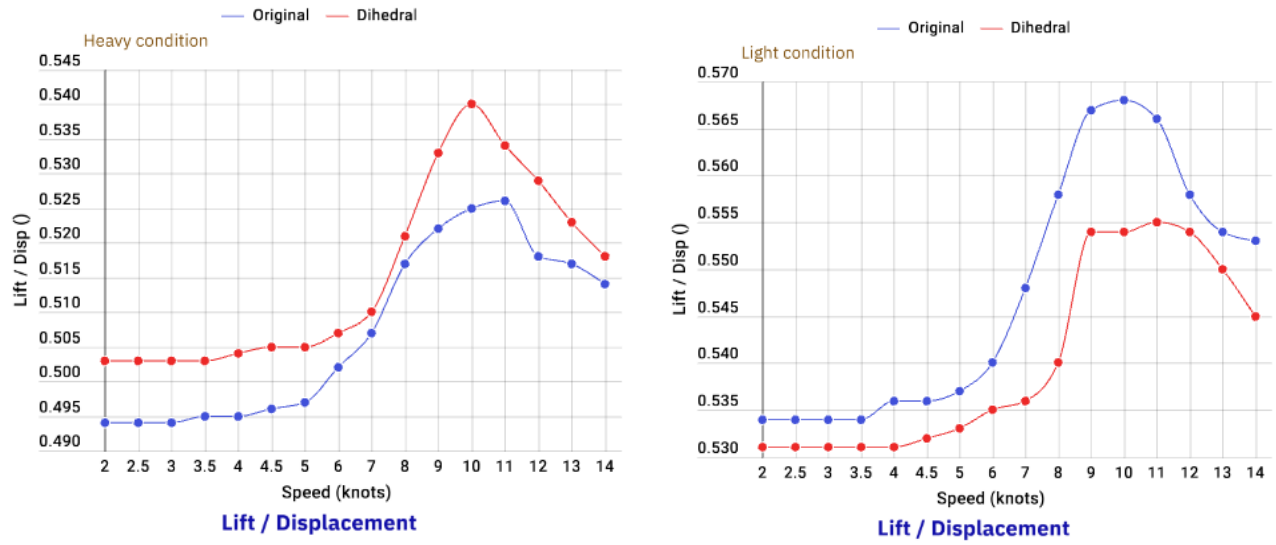

(a) heavy-load condition

(b) light-load condition

Figure 13: Lift-to-displacement ratio for the original and dihedral bulbous bow configurations: (a) heavy-load condition; (b) light-load condition.

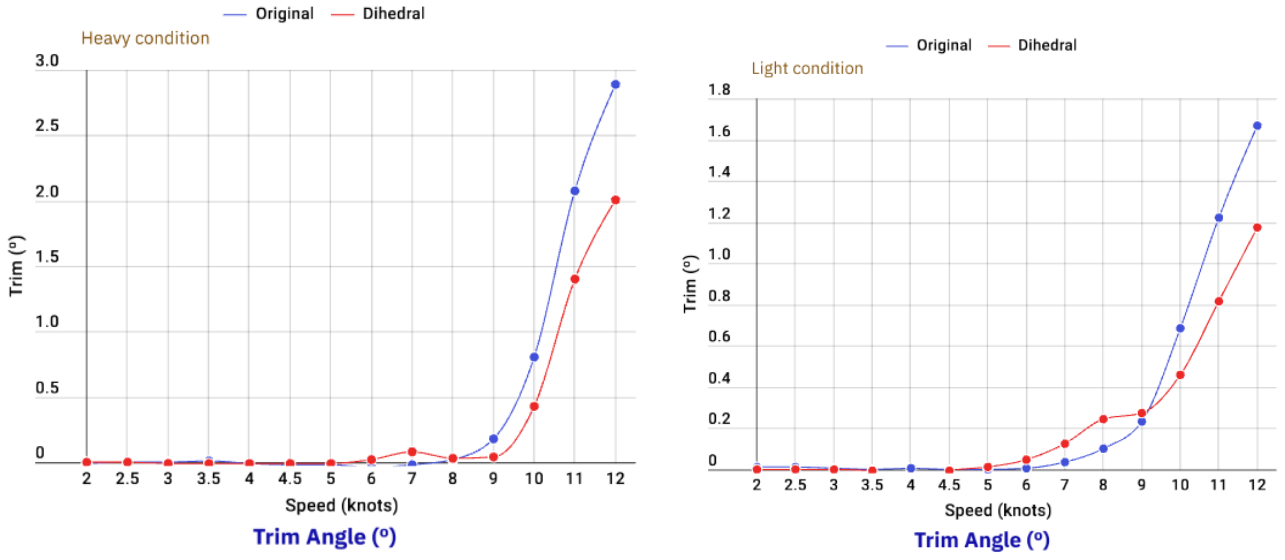

(a) light-load condition

(b) heavy-load condition

Figure 14: Trim angle comparison for the original and dihedral bulbous bow configurations: (a) light-load condition; (b) heavy-load condition.

threshold beyond which the dihedral bulbous bow provides consistent trim reduction benefits—slightly higher than the 7-knot threshold identified for resistance reduction. Beyond 9 knots, the combined benefits of reduced resistance and reduced trim make the dihedral bulbous bow retrofit highly advantageous for high-speed operation under heavy-load conditions.

In semi-planing vessels, the hydrodynamic behavior of the bow region is strongly influenced by the interaction between hydrodynamic lift and trim, rather than by buoyancy alone. As speed increases, the development of pressure-induced lift on the hull bottom promotes bow emergence through dynamic trim, effectively reducing the wetted length of the forward hull. This process fundamentally alters the pressure field and the wave pattern generated by the vessel. The presence of a bulbous bow in this regime introduces

an additional mechanism. Beyond its classical role in wave interference, the bulb produces a virtual longitudinal extension of the forebody, modifying the effective flow incidence and the pressure recovery along the forward bottom. As the hull trims and partially emerges, this virtual lengthening modify flow separation and redistributes the high-pressure region responsible for lift generation differently. As a consequence, the lift generated in semi-planing conditions is directly coupled with trim: increased lift induces trim changes, which in turn modify the local angle of attack and the pressure distribution over both the hull and the bulb. This feedback mechanism leads to a reorganization of the wave system, characterized by shifts in wave crest location and amplitude that are not observed in displacement hulls that is also influences by a virtual longitunal extension of the hull. In contrast, for displacement vessels the hull remains fully supported by buoyancy, trim variations are limited, and the bulb primarily affects wave-making through linear interference mechanisms. The strong coupling between lift, trim, and wave pattern observed here is therefore intrinsic to semi-planing operation and explains the markedly different hydrodynamic response compared to displacement regimes.

4.6. Experimental Flow Visualisation

This section presents qualitative flow visualisation results from the towing tank experiments, providing physical insight into the mechanisms by which the dihedral bulbous bow alters the flow field and reduces hydrodynamic resistance. For conciseness, corresponding CFD visualisations are not included here, as quantitative agreement has already been demonstrated in the validation section. Although the comparisons are qualitative, they clearly illustrate the redistribution of flow around the hull following bulb integration and, when considered in conjunction with the force and trim data presented previously, elucidate the physical mechanisms responsible for performance improvement.

The fundamental mechanism is geometric: the dihedral bulbous bow effectively lengthens the waterline and redistributes the bow pressure field, thereby modifying wave generation and hull-water interaction. This altered pressure distribution leads to reduced wave-making resistance whilst simultaneously affecting trim and lift. These effects are illustrated in Figures 15 and 16 for the light-load and heavy-load conditions, respectively, at three representative speeds: 6, 8, and 11 knots, corresponding to displacement, transitional, and semi-planing regimes.

4.6.1. Light-load

condition Observations (Figure 15)

6 knots (Fr = 0.25, displacement regime): At this speed, the dihedral bulbous bow provides no measurable resistance benefit. Water is deflected aft of station 8 in both configurations, and the flow redirected by the dihedral bulbous bow reattaches to the hull rather than being cleanly separated. The wetted surface area is larger for the dihedral bulbous bow configuration due to the additional immersed bulb surface, and trim is slightly higher (approximately 0.3° compared to near-zero for the baseline). The lack of benefit at this Froude number confirms that bulbous bows are ineffective in the displacement regime for this hull form.

8 knots (Fr = 0.34, transitional regime): The dihedral bulbous bow begins to demonstrate modest resistance reduction of approximately 1–3%. In the baseline hull, water is deflected laterally from approximately station 10, whilst in the dihedral bulbous bow configuration the deflection originates near station 11, indicating that the bow wave system has been displaced forward. The hull remains dry up to station 8 in the dihedral bulbous bow configuration, suggesting reduced spray and a cleaner pressure recovery region. Trim is essentially 0° for the baseline hull and 0.2° for the dihedral bulbous bow configuration—both negligible values indicating that dynamic lift has not yet become significant.

11 knots (Fr = 0.47, semi-planing regime): At this speed, the dihedral bulbous bow achieves substantial resistance reduction of approximately 19–28%. In the baseline hull, water is deflected from station 10, whereas in the dihedral bulbous bow configuration deflection begins at station 10.5, and the hull remains dry forward of station 8. The wetted area above the chine near station 8 is noticeably larger for the baseline hull, indicating that the dihedral bulbous bow has reduced spray and altered the pressure distribution to keep the forward sections dry. Trim is 1.4° for the baseline hull and 1.0° for the dihedral bulbous bow configuration—a 0.4° reduction that, whilst modest in absolute terms, represents a 29% decrease and contributes to the reduced resistance through decreased wetted surface area.

4.6.2. Heavy-load

condition Observations (Figure 16) **6 knots (Fr = 0.25, displacement regime):** Similar to the light-load condition, the dihedral bulbous bow provides no resistance benefit at this low Froude number. Water is deflected upstream of station 8 in both configurations, and flow redirected by the bulb reattaches to the hull. The wetted surface area is greater for the dihedral bulbous bow configuration, and trim is slightly elevated. This confirms that the bulbous bow is ineffective—or even slightly detrimental—in the displacement speed regime regardless of loading condition.

8 knots (Fr = 0.34, transitional regime): The dihedral bulbous bow achieves substantial resistance reduction of approximately 11–16%—significantly greater than the 1–3% observed under light-load condition at the same speed. In the baseline hull, water is deflected from station 10, whereas in the dihedral bulbous bow configuration deflection begins at station 11, and the deflected flow does not impinge on the hull forward of station 8. Trim is nearly 0° for both configurations, but the flow pattern appears noticeably cleaner for the dihedral bulbous bow configuration, with reduced spray and a more organised wave system. This indicates that the deeper immersion of the bulb at heavy-load condition enhances its wave interference effect.

11 knots (Fr = 0.47, semi-planing regime): The dihedral bulbous bow reduces resistance by approximately

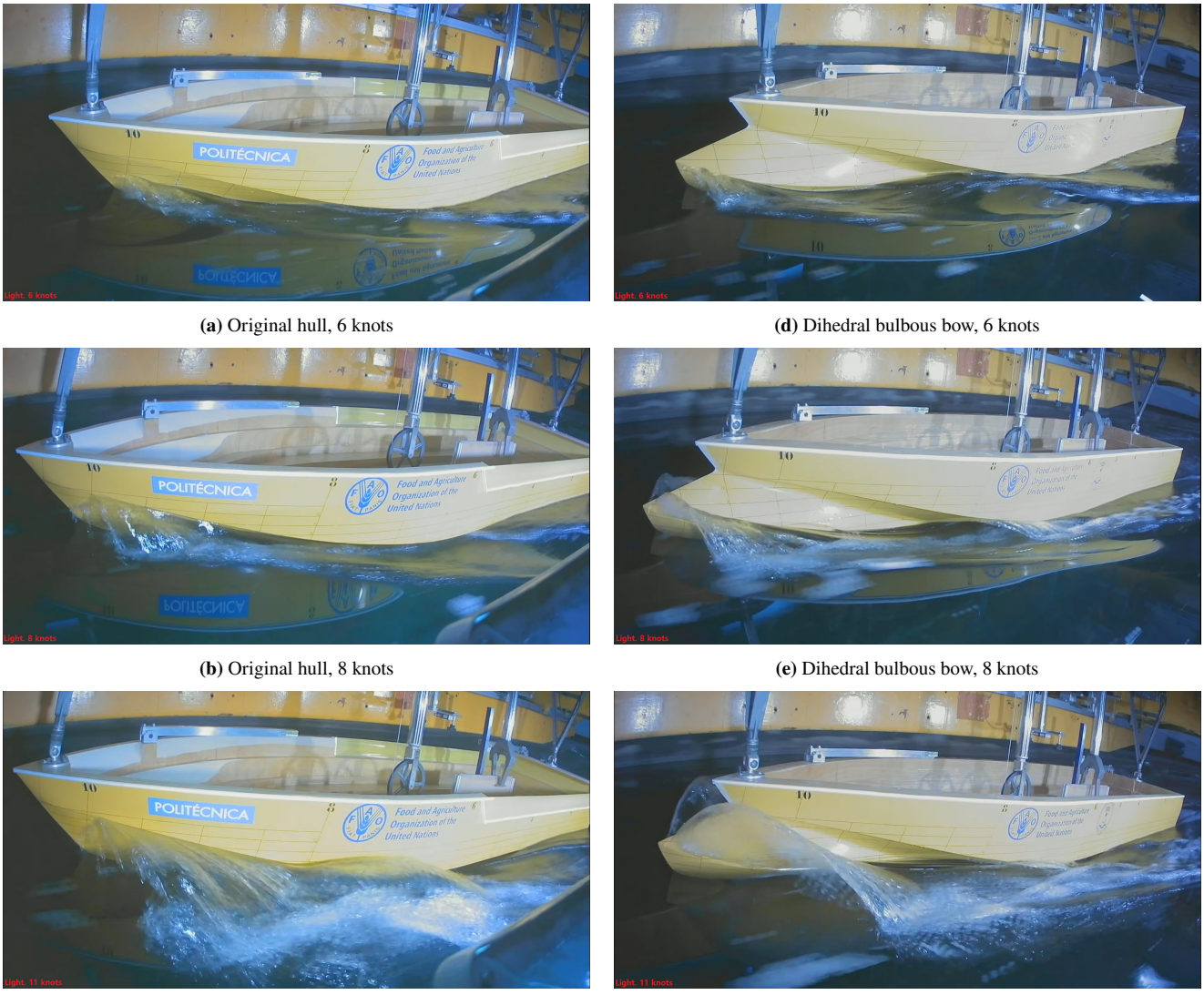

(a) Original hull, 6 knots

(d) Dihedral bulbous bow, 6 knots

(b) Original hull, 8 knots

(e) Dihedral bulbous bow, 8 knots

(c) Original hull, 11 knots

(f) Dihedral bulbous bow, 11 knots

Figure 15: Experimental images of the hull in the light-load condition at speeds of 6, 8, and 11 knots, comparing the original hull (left) and the dihedral bulbous bow (right).

18–32%—the largest benefit observed in this study. In the baseline hull, water deflection originates at station 10, whilst in the dihedral bulbous bow configuration it begins at station 11, maintaining the hull dry forward of station 9. The wetted area above the chine near station 9 is substantially larger for the baseline hull. Trim is 2.3° for the baseline hull and 1.5° for the dihedral bulbous bow configuration—a 0.8° (35%) reduction that significantly contributes to resistance reduction by decreasing wetted surface area and improving propeller immersion. The combination of reduced wave-making, cleaner flow separation, and trim reduction produces the maximum performance benefit at this condition.

4.7. Hydrostatic overview

The inclusion of a bulbous bow leads to slight modifications of the hull form coefficients, with the most significant effects being observed in the waterplane characteristics (Table 5). The prismatic coefficient, C_P, is primarily reduced as a consequence of the increase in waterline length under both loading conditions. This reduction indicates that the vessel fitted with a bulbous bow presents a lower apparent volume concentration in the bow region when compared with the original hull forms. In addition, the waterplane coefficient, C_{WP}, decreases considerably, resulting in a more slender hull form relative to the original configurations. Furthermore, the ratio LCB/LWL exhibits a slight reduction for the bulbous-bow configurations, while the ratio LCF/LWL shows a more pronounced decrease. This behavior confirms a finer waterline geometry with the longitudinal centroid shifted aft when compared with the original hull forms.

5. Discussion and Conclusions

This investigation has demonstrated the hydrodynamic performance improvements achievable through retrofit integration of a dihedral bulbous bow onto a semi-planing

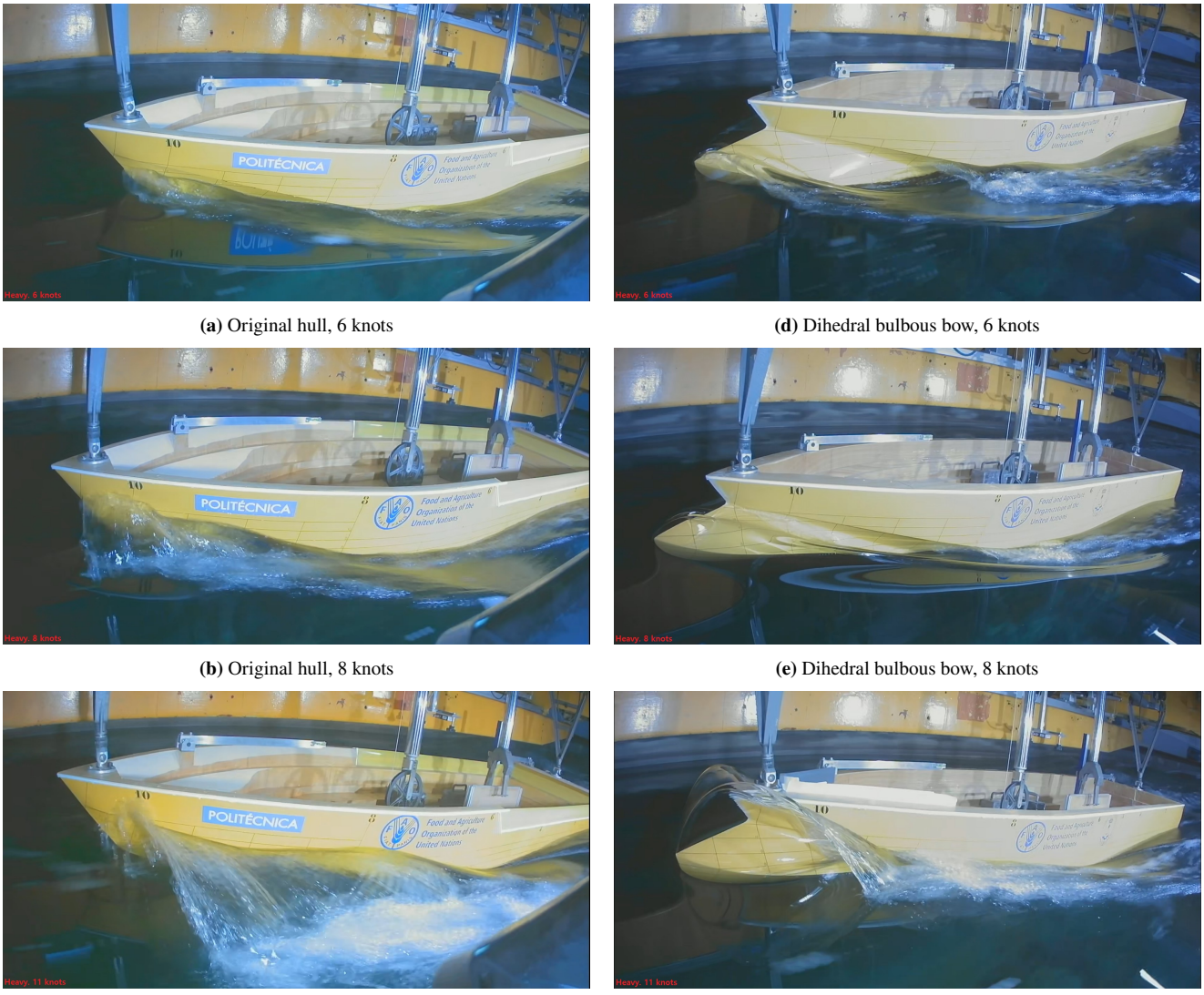

(a) Original hull, 6 knots

(d) Dihedral bulbous bow, 6 knots

(b) Original hull, 8 knots

(e) Dihedral bulbous bow, 8 knots

(c) Original hull, 11 knots

(f) Dihedral bulbous bow, 11 knots

Figure 16: Experimental images of the hull in the heavy-load condition at speeds of 6, 8, and 11 knots, comparing the original hull (left) and the dihedral bulbous bow (right).

Table 5
Hydrostatic characteristics of the hull

Condition	C_B	C_X	C_P	C_{WP}	LCB/LWL	LCF/LWL
Heavy Condition						
No Bulb	0.33	0.42	0.80	0.84	0.44	0.44
Bulb	0.32	0.42	0.77	0.79	0.43	0.42
Light Condition						
No Bulb	0.23	0.30	0.78	0.81	0.46	0.43
Bulb	0.23	0.30	0.76	0.76	0.45	0.41

artisanal fishing vessel through combined experimental and numerical analysis. The comprehensive dataset obtained enables assessment of both the magnitude of performance benefits and identification of the operational regimes where retrofit implementation is most advantageous.

Validation of the CFD methodology against experimental measurements yielded mean prediction errors below 6% for resistance, with deviations exceeding 3% occurring only at isolated test conditions. Dynamic trim predictions similarly exhibited close agreement with experimental data across the speed range, with typical errors below 0.5° in trim angle. This level of accuracy establishes confidence in the RANS-VOF approach as a reliable tool for performance assessment of semi-planing hulls, complementing physical model testing whilst providing access to detailed flow field information not readily obtainable through experimentation. The validated numerical framework enables investigation of additional hull modifications, loading conditions, or operational scenarios without the time and cost constraints of towing tank testing, significantly expanding the scope of parametric design studies.

From a hydrodynamic performance perspective, the dihedral bulbous bow retrofit demonstrates effectiveness specifically within the transitional and semi-planing speed

regimes. Below approximately 7 knots (Fr < 0.30), both hull configurations exhibit nearly identical resistance characteristics, with differences falling within experimental uncertainty. This behaviour is consistent with established bulbous bow theory, which predicts minimal benefit in the displacement regime where wave-making resistance is a small fraction of total resistance and where the bulb's wave interference mechanism cannot operate effectively. Beyond the 7-knot threshold, however, resistance divergence becomes pronounced and increases progressively with speed.

Under light-load condition, the dihedral bulbous bow achieves maximum resistance reduction of 28% at 11 knots, whilst under heavy-load condition the maximum benefit of 32% occurs at 10 knots. These substantial improvements persist at higher speeds, though diminishing slightly to approximately 15–19% at 14 knots (Fr $= 0.59$). The resistance reduction is attributable primarily to decreased pressure resistance resulting from favourable wave interference and altered bow pressure distribution, as evidenced by the force decomposition analysis. Viscous resistance remains essentially unchanged between configurations across the speed range, confirming that the bulb does not incur a frictional penalty despite the modest increase in wetted surface area. This indicates that the geometric design of the dihedral bulbous bow—with its developable surface and gradual integration into the parent hull—successfully minimises viscous effects whilst optimising pressure field modification.

The heavier displacement condition consistently demonstrates greater resistance reduction than the light-load condition at equivalent Froude numbers, particularly within the 8–11 knot speed range. This displacement sensitivity likely arises from two factors: first, the bulb is more deeply immersed at heavy-load condition, enhancing its wave-making influence; and second, the baseline hull's wave-making resistance is proportionally larger at heavy-load condition, providing greater scope for improvement through favourable wave interference. This finding has practical implications for vessel operators, as the retrofit provides maximum benefit precisely during the loaded departure condition when fuel consumption is highest.

Analysis of vertical hydrodynamic lift forces reveals displacement-dependent behaviour that provides insight into the physical mechanisms governing trim and emergence. Under light-load condition, the baseline hull generates greater lift than the dihedral bulbous bow configuration across most of the speed range, suggesting that the bulb modifies the bow pressure distribution in a manner that reduces vertical force whilst simultaneously reducing resistance. This represents a favourable trade-off for vessels that do not require maximum dynamic lift for planing. Under heavy-load condition, the trend reverses: the dihedral bulbous bow produces substantially greater lift, reaching a pronounced maximum near 10 knots—close to the threshold of fully-developed planing conditions. This increased lift aids in supporting the greater displacement whilst simultaneously reducing wave-making resistance, demonstrating the complex interplay between vertical and longitudinal force components in semi-planing hulls.

Dynamic trim behaviour exhibits two characteristic transition speeds: approximately 7 knots, where resistance divergence commences, and approximately 9 knots, where significant differences in trim behaviour emerge. For light-load condition, the dihedral bulbous bow initially produces marginally higher trim between 6 and 9 knots—likely associated with the altered longitudinal pressure distribution and forward shift of the centre of pressure. Beyond 9 knots, however, the dihedral bulbous bow configuration consistently exhibits lower trim than the baseline hull, with differences increasing progressively with speed. Under heavy-load condition, this trend is more pronounced: whilst both configurations maintain negligible trim below 8 knots, the baseline hull develops extreme bow-up attitudes exceeding 13° at 12 knots, whereas the dihedral bulbous bow configuration maintains substantially lower trim throughout the semi-planing regime.

The observed trim reduction has direct operational benefits beyond the primary resistance reduction. Lower trim angles improve propeller immersion and reduce ventilation risk, enhance directional stability, reduce wetted surface area by keeping aft sections submerged, and improve crew comfort and safety by maintaining a more level deck attitude. These benefits are particularly significant for fishing vessels, where deck operations, gear handling, and crew movement are integral to vessel function.

Experimental flow visualisation qualitatively confirms the numerical predictions and elucidates the physical mechanisms underlying the observed performance improvements. The dihedral bulbous bow delays the lateral deflection of water along the hull—shifting the spray root aft by approximately one station—and maintains drier hull surfaces forward of stations 8–9 depending on speed and displacement. At 11 knots under light-load condition, for example, the baseline hull exhibits substantial spray and wetted area above the chine near station 8, whilst the dihedral bulbous bow configuration maintains these surfaces dry with a cleaner, more organised flow separation. These flow field modifications translate directly to reduced pressure drag through decreased form resistance and favourable wave interference.

The identification of critical transition speeds at 7 and 9 knots has important operational implications for vessel design and retrofit decision-making. Artisanal fishing vessels typically operate across a broad speed range: low speeds (3–6 knots) during fishing operations and gear deployment, and higher speeds (8–12 knots) during transit to and from fishing grounds. The dihedral bulbous bow retrofit provides minimal benefit during low-speed operations but yields substantial improvements during high-speed transit—precisely the regime where fuel consumption and power demand are greatest. For a vessel operating 40% of its time at low speed and 60% at high speed, the weighted-average resistance reduction would be approximately 12–15%, translating to proportional reductions in fuel consumption, operating costs, and greenhouse gas emissions.

From an economic perspective, the dihedral bulbous bow retrofit represents a cost-effective alternative to new vessel construction. The developable surface geometry enables fabrication using conventional boatbuilding techniques accessible to small shipyards in developing regions, without requiring sophisticated compound-curvature forming capabilities or advanced materials. The retrofit can be implemented during routine maintenance periods without extensive structural modification to the parent hull, minimising downtime and installation costs. When combined with the demonstrated fuel savings, the retrofit investment can achieve payback periods of 2–4 years depending on vessel utilisation and fuel prices—a compelling economic proposition for small-scale fishing operations.

The environmental benefits are equally substantial. A reduction in fuel consumption directly translates into lower greenhouse gas emissions, thereby advancing the decarbonisation objectives established under international maritime environmental frameworks. For artisanal fishing fleets comprising hundreds or even thousands of vessels, the widespread implementation of cost-effective efficiency enhancements—such as bulbous bow retrofits—has the potential to deliver significant cumulative emissions reductions without necessitating fleet replacement or the adoption of alternative propulsion technologies.

Several limitations of the present study should be acknowledged. The investigation was conducted exclusively in calm water conditions without consideration of seakeeping performance in waves, which represents a significant portion of operational time for offshore fishing vessels. The added bow volume and modified waterline may affect wave-induced motions, slamming loads, and green water shipping, requiring evaluation through seakeeping model tests or numerical simulations in regular and irregular waves. Additionally, the study examined only two discrete loading conditions; performance across the full operational displacement range—including intermediate loadings and asymmetric conditions—would provide a more complete characterisation. Finally, the investigation focused on a single bulb geometry; systematic parametric optimisation of bulb dimensions, longitudinal position, and sectional shape could potentially yield further performance improvements.

Future research directions include: experimental and numerical investigation of seakeeping performance with the dihedral bulbous bow in representative sea states; parametric optimisation of bulb geometry using formal optimisation algorithms coupled with CFD; evaluation of self-propulsion characteristics including propeller-hull interaction effects; assessment of manoeuvring performance and directional stability; and full-scale trials on an instrumented vessel to validate model-scale predictions and quantify real-world fuel savings under operational conditions.

In conclusion, the integration of a dihedral bulbous bow onto a semi-planing artisanal fishing vessel has demonstrated substantial hydrodynamic performance improvements at medium and high speeds, including resistance reductions of 28–32% at operationally significant speeds, favourable trim reduction improving vessel dynamics, and beneficial flow field modifications confirmed through experimental visualisation. These improvements are achieved without viscous penalties and are most pronounced under heavy-load conditions when fuel consumption is greatest. The results establish bulbous bow retrofitting as a practical, cost-effective, and environmentally beneficial strategy for improving the efficiency of existing artisanal fishing vessels, with particular relevance to developing regions where new construction is economically prohibitive and where small improvements in fuel efficiency yield disproportionate benefits to fishing communities. The validated numerical methodology provides a reliable framework for evaluating additional hull modifications and supports the broader objective of enhancing the sustainability and economic viability of small-scale fisheries.

CRediT authorship contribution statement

H. R. Díaz-Ojeda: Validation, Investigation, Funding acquisition, Writing - Original Draft, Writing - review. **Yifu Zhang:** Validation, Investigation, Writing - Original Draft. **Tahsin Tezdogan:** Investigation, Writing - Original Draft, Writing - review. **Francisco Pérez Arribas:** Conceptualization, Investigation, Funding acquisition, Writing - review, Supervision.

Declaration of Competing Interest

The authors declare that they have no known competing financial interests or personal relationships that could have appeared to influence the work reported in this paper.

Acknowledgement

The authors acknowledge the use of the IRIDIS High Performance Computing Facility, and associated support services at the University of Southampton, in the completion of this work. Authors also acknowledges the funding provided by the Ministerio de Ciencia e Innovación through grant PID2022-140481OB-I00. FAO , with support from the Norwegian Government funded Trust Fund project GCP/GLO/352/NOR, introduced the bulbous bow as a fuel saving exercise in 2023.

Data availability

The data that support the findings of this study are available from the corresponding author upon reasonable request.

References

[1] Bentin, M., Kotzur, S., Schlaak, M., Zastrau, D., Freye, D., 2018. Perspectives for a wind assisted ship propulsion. International Journal of Maritime Engineering doi:10.3940/RINA.IJME.2018.A1.439.

[2] Díaz-Ojeda, H., Pérez-Arribas, F., Turnock, S.R., 2023. The influence of dihedral bulbous bows on the resistance of small fishing vessels: A numerical study. Ocean Engineering 281, 114661. URL: https:

//www.sciencedirect.com/science/article/pii/S0029801823010454, doi:https://doi.org/10.1016/j.oceaneng.2023.114661.

[3] Díaz Ojeda, H.R., Oyuela, S., Sosa, R., Otero, A.D., Pérez Arribas, F., 2024. Fishing vessel bulbous bow hydrodynamics—a numerical reverse design approach. Journal of Marine Science and Engineering 12. URL: https://www.mdpi.com/2077-1312/12/3/436, doi:10.3390/jmse12030436.

[4] European Economic and Social Committee (EESC), 2023. Decarbonisation of the fishing fleet. https://www.eesc.europa.eu/en/our-work/opinions-information-reports/opinions/decarbonisation-fishing-fleet. Adopted 12 July 2023. Consultado el February 24, 2026.

[5] FAO Fisheries & Aquaculture, n.d.a. Grd-15: Vessel design. https://www.fao.org/fishery/en/vesseldesign/grd-15.

[6] FAO Fisheries & Aquaculture, n.d.b. Vessel design search. https://www.fao.org/fishery/en/vesseldesign/search.

[7] Hollenbach, I.U., Chryssostomidis, C., Johansson, K., 1999. Estimating resistance and propulsion for single-screw and twin-screw ships in the preliminary design. Massachusetts Institute of Technology, MIT Sea Grant College Program.

[8] Holtrop, J., Mennen, G., 1982. An approximate power prediction method. International shipbuilding progress 29, 166–170.

[9] Hoyle, J., Cheng, B., Hays, B., Johnson, B., Nehrling, B., 1986. Bulbous bow design methodology for high-speed ships. 94, 31–56.

[10] Iqbal, M., Terziev, M., Tezdogan, T., Incecik, A., 2025. Hull form optimisation to minimise the total resistance and dynamic responses of small fishing vessels. Ocean Engineering 321, 120357. URL: https://www.sciencedirect.com/science/article/pii/S0029801825000721, doi:https://doi.org/10.1016/j.oceaneng.2025.120357.

[11] 28th ITTC Quality Systems Group, 2017. ITTC - General Guidelines for Uncertainty Analisys in Resistance Tests. ITTC.

[12] 26th ITTC Resistance Committee, 2011. ITTC – Recommended Procedures and Guidelines - Resistance Test. ITTC.

[13] Kracht, A.M., 1978. Design of bulbous bows. Technical Report.

[14] Kyriazis, G., 1996. Bulbous bow design optimization for fast ships .

[15] Mahmoudi, M., Saboohi, Y., Köhler, J., 2024. Facilitating the transition to sustainable propulsion in the shipping industry: An agent-based modelling analysis of retrofitting. Environmental Innovation and Societal Transitions 51, 100838. URL: https://www.sciencedirect.com/science/article/pii/S2210422424000297, doi:https://doi.org/10.1016/j.eist.2024.100838.

[16] Pérez-Arribas, F., Silva-Campillo, A., Díaz-Ojeda, H.R., 2022. Design of dihedral bows: A new type of developable added bulbous bows—experimental results. Journal of Marine Science and Engineering 10. URL: https://www.mdpi.com/2077-1312/10/11/1691, doi:10.3390/jmse10111691.

[17] Specialist Committee: Procedures for Resistance, P., of 23rd ITTC 2002, P.O.W.T., 2002. ITTC – Recommended Procedures and Guidelines: Model Manufacture, Ship Models. ITTC.

[18] Rotteveel, E., Hekkenberg, R., van der Ploeg, A., 2017. Inland ship stern optimization in shallow water. Ocean Engineering 141, 555–569. URL: https://www.sciencedirect.com/science/article/pii/S0029801817303232, doi:https://doi.org/10.1016/j.oceaneng.2017.06.028.

[19] Saral, D., 2024. The effect of various bulbous bow forms on the resistance of a black sea type fishing boat. Seatific Journal 4, Article 2. URL: https://commons.yildiz.edu.tr/seatific/vol4/iss2/2, doi:10.29187/2792-0771.1029.

[20] Szelangiewicz, T., Abramowski, T., Żelazny, K., Sugalski, K., 2021. Reduction of resistance, fuel consumption and ghg emission of a small fishing vessel by adding a bulbous bow. Energies 14. URL: https://www.mdpi.com/1996-1073/14/7/1837, doi:10.3390/en14071837.

[21] Tavakoli, S., Zhang, M., Kondratenko, A.A., Hirdaris, S., 2024. A review on the hydrodynamics of planing hulls. Ocean Engineering 303, 117046. URL: https://www.sciencedirect.com/science/article/pii/S0029801824003834, doi:https://doi.org/10.1016/j.oceaneng.2024.117046.

[22] Zhang, S., Tezdogan, T., Zhang, B., Xu, L., and, Y.L., 2018. Hull form optimisation in waves based on cfd technique. Ships and Offshore Structures 13, 149–164. URL: https://doi.org/10.1080/17445302.2017.1347231, doi:10.1080/17445302.2017.1347231, arXiv:https://doi.org/10.1080/17445302.2017.1347231.